Universidad de Concepción
Dirección de Postgrado
Facultad de Ciencias Físicas y Matemáticas
Programa de Doctorado en Ciencias Físicas

INFLUENCE OF OCEANIC PROCESSES IN THE LOCAL MAGNETIC FIELD

POR

CARLOS ESTEBAN TORRES ECHEVERRÍA

Tesis presentada a la
Facultad de Ciencias Físicas y Matemáticas de la Universidad de Concepción
para optar al grado académico de Doctor en Ciencias Físicas

Profesor Guía : Dr. Dante Figueroa Martínez

Comisión : Dr. Óscar Roberto Pizarro Arriagada
Dr. Rafael Enrique Aránguiz Muñoz

Diciembre de 2019
Concepción, Chile

A Cristina.

AGRADECIMIENTOS

En primer lugar, quiero agradecer tanto a la Comision Nacional de Investigación Científica y Tecnológica (CONICYT), por financiar el desarrollo de esta tesis mediante la beca CONICYT-PFCHA/DOCTORADO NACIONAL/2015-21150632, como a la Dirección de Postgrado de la Universidad de Concepción, por aprobar el plazo necesario para poder finalizar con éxito mi investigación.

Extiendo mis agradecimientos al Director del Programa de Doctorado en Ciencias Físicas, Dr. Jaime Araneda, y a todo el Personal del Departamento de Física, por tener siempre buena disposición cuando lo necesité. Al Dr. Luis Roa y al Centro de Estudiantes de Postgrado en Física (CEPFis), por ayudarme a conseguir un puesto de estudio en la Facultad. También agradezco al Departamento de Ingeniería Matemática, por permitirme realizar el análisis de datos necesario para el primer artículo en su Laboratorio de Cálculo Científico.

Agradezco enormemente a la Dra. Ignacia Calisto y al Dr. Óscar Pizarro, del Departamento de Geofísica (DGEO), con quienes trabajé en los dos artículos que sustentan esta tesis; fue un agrado y me llevo un muy buen recuerdo. Al Dr. Matt Miller, como Director del DGEO, por su ayuda con el primer artículo y por apoyarme para ir a mostrar algunos resultados de esta tesis al II Congreso de Jóvenes Investigador⋆s del Mar, en España. A todos los integrantes del DGEO, por su compañerismo y por hacerme sentir como en casa.

En forma especial, agradezco al Dr. Dante Figueroa por estos años de colaboración. Por aceptar ser mi tutor, y por todo el tiempo que le dedicó tanto al estudiante como a la persona. Por sobre todo, le agradezco por hacer que el doctorado fuese una gratificante experiencia de vida. Finalmente, le agradezco a él, al Dr. Óscar Pizarro y al Dr. Rafael Aránguiz por formar parte de la comisión de evaluación de esta tesis.

A mis amigos, a los de hace años y a los nuevos, por su compañía. Entre estos últimos, quisiera destacar a mis amigos de la Parroquia Del Sagrario y nuestras reuniones de los lunes, indispensables para comenzar la semana con energía. Una mención especial a Vicki, tanto por su amistad como por sus incontables correcciones a mis frases en inglés.

Agradezco a mi familia, en general, por su cariño y compañía; en especial a Karla y Cristian. A mi madre, por su apoyo incondicional sobre todo en la última etapa del doctorado y por creer siempre en mi; sin ella, estas páginas estarían en blanco.

A todos los colegas, profesores y amigos que con sus sugerencias, consejos y críticas hicieron posible que esta tesis se realizara.

TABLE OF CONTENTS

ABBREVIATIONS

CHIOOS	Chilean Integrated Ocean Observing System
CInFAA	Centro Interuniversitario de Física de la Alta Atmósfera
CMEMS	Copernicus Marine and Environment Monitoring Service
COMCOT	COrnell Multi-grid COupled Tsunami
DART	Deep-ocean Assessment and Reporting of Tsunamis
IPM	Isla de Pascua Mataveri
INTERMAGNET	International Real-time Magnetic Observatory Network
LAI	litosphere-atmosphere-ionosphere
LHS	left-hand side
LSW	linear shallow water
nT	nanotesla
NSW	nonlinear shallow water
OGM	ocean-generated magnetic
OMCT	Ocean Model for Circulation and Tides
PM	poloidal mode
RHS	right-hand side
RMSE	Root Mean Squared Error
SAMBA	South American Meridional B-Field Array
SLA	Sea level anomaly
TAI	tsunami-atmosphere-ionosphere
TGM	tsunami-generated magnetic
TIME-GCM	Thermosphere Ionosphere Mesosphere Electrodynamics General Circulation Model
TM	toroidal mode
UTC	Coordinated Universal Time

LIST OF TABLES

LIST OF FIGURES

ABSTRACT

As the electrically-conducting seawater flows across the Earth's magnetic field, the moving salt ions are deflected by their interaction with the geomagnetic field, thereby inducing electric currents in the ocean. These currents generate secondary magnetic fields, in the range of the nanotesla (nT), which are measurable outside of the ocean layer at land-based magnetic observatories.

The goal of this thesis is to investigate the presence of ocean-generated magnetic perturbations in geomagnetic data recorded at an observatory located in Easter Island, Chile (about 3500 km west of Chilean coast) in two cases: tsunamis and ocean circulation. The methodology used to accomplish the objective involves to compare magnetic records from the Easter Island Observatory with modelled magnetic disturbances for three time periods: during the 2010 and 2015 Chilean earthquake-induced tsunamis, and during the 2011-2015 period. The computed magnetic fields are obtained by combining ocean velocities, from numerical tsunami simulations and satellite altimeter data, with the Biot-Savart law in a rectangular area around Easter Island.

The results of the modelling are in good agreement, in specific period bands, with the observed perturbations in the vertical component of the geomagnetic field. The results reveal that even a small tsunami, such as the one produced by the 2015 Mw8.2 earthquake, induces an observable magnetic perturbation due to the water movement. The results also indicate that not only mesoscale but also large-scale marine currents around Easter Island are suitable to be monitored, since even electric

currents at great distances from the observatory are of importance for the induced field there.

This study shows that the influence of marine currents in the Earth's magnetic field is significant, that this physical process can be adequately described with accessible numerical tools, and that it can be an instrument for monitoring the ocean, whether on minute (tsunamis) or monthly and larger (ocean circulation) timescales.

RESUMEN

A medida que el agua de mar -eléctricamente conductora- se mueve a través del campo magnético de la Tierra, los iones de sodio y cloro disueltos en el océano son desviados debido a su interacción con este campo y su movimiento induce corrientes eléctricas en el océano. Estas corrientes generan campos magnéticos secundarios, en el orden de los nanotesla, medibles fuera de la capa oceánica en observatorios magnéticos instalados en tierra.

El objetivo de esta tesis es investigar la presencia de perturbaciones generadas por el océano en datos geomagnéticos registrados en un observatorio ubicado en la Isla de Pascua, Chile, para dos casos: tsunamis y circulación oceánica. La metodología consiste en comparar los datos del observatorio con los resultados de un modelo numérico en tres períodos de tiempo: durante los tsunamis de 2010 y 2015, provocados por terremotos en Chile, y durante el período 2011-2015. El modelo numérico es calculado a partir de la ley de Biot-Savart y velocidades oceánicas en un área rectangular alrededor de la Isla de Pascua. Las velocidades son obtenidas de simulaciones numéricas de tsunamis y datos de altimetría satelital.

Los resultados de la modelación coinciden en bandas de período específicas con los datos de la componente vertical del campo geomagnético e indican que incluso un tsunami pequeño, como el producido por el terremoto Mw8.2 de 2015, induce una perturbación observable debido al movimiento del agua. Los resultados también

indican que tanto las corrientes marinas de mesoescala como las de gran escala alrededor de la isla podrían ser monitoreadas, ya que incluso corrientes eléctricas a grandes distancias del observatorio contribuyen al campo inducido.

Este estudio muestra que la influencia de las corrientes marinas en el campo magnético terrestre es significativa, que este proceso físico puede describirse adecuadamente con herramientas numéricas accesibles, y que puede constituir un instrumento para monitorear el océano, ya sea en escala temporales de minutos (tsunamis), o bien mensuales o mayores (circulación oceánica).

Chapter 1

INTRODUCTION

The hydrated sodium and chloride ions dissolved in the sea constitute the vast majority of the charge carriers contributing to the electrical conductivity of the ocean. As the electrically-conducting seawater flows through the Earth's magnetic field, the salt ions are deflected by their interaction with this field, thereby establishing a motional electromotive force which drives electric currents in the sea. These currents induce small, but detectable, magnetic fields[1], in the range of a few nanotesla (nT), circling around them. These OGM perturbations are observable at land-based geomagnetic stations, on the seafloor, and even at low-Earth-orbiting satellites (Larsen 1968 [32]; Minami 2017 [42]). Various ocean processes, such as internal waves (Pukhtyar and Kukushkin 1996 [52]), mesoscale eddies (Lilley et al. 1993 [36]), tsunamis (Tatehata et al. 2015 [61]), semi-diurnal and diurnal tides (Larsen 1968 [32]; Tyler et al. 2003 [67]; Saynisch et al. 2017 [56]; Schnepf et al. 2018 [59]) and circulation (Manoj et al. 2006 [37]; Saynisch et al. 2018 [55]), among others, produce detectable magnetic signals. Nowadays, even developing El Niño–Southern Oscillation events can be found in oceanic induced magnetic fields (Petereit et al. 2018 [48]).

The importance of monitoring the geomagnetic field can be illustrated with some

[1]Hereafter, the expression "OGM" is used to abbreviate "ocean-generated magnetic".

examples:

- Geomagnetic storms can disrupt our global electric power distribution and radio communication systems (Gonzalez et al. 1994 [17]).
- Some authors (Minami et al. 2015 [46]; Schnepf et al. 2016 [58]; Minami et al. 2019 [43]) state that during a tsunami event, the OGM signals could even precede the arrival of the tsunami waves.
- Ocean temperature and salinity are the major variables that determine the electrical conductivity of the seawater, and measurements of the geomagnetic field contain nearly global information about combined transports of water, heat, and salinity in the ocean (Tyler et al. 1999 [68]; Irrgang et al. 2019 [22]).

From the aforementioned examples, tsunamis are specially relevant for our country: the Pacific Ocean is considered the most tsunami-dangerous region, and earthquakes are repeatedly occurring around the perimeter of the ocean inside the so-called Ring of Fire (Levin and Nosov 2016 [34]). Tsunami-generated magnetic (TGM) signals recorded at ground magnetometers can be produced by electric currents not only in the ocean but also in the ionosphere, the region of the atmosphere from about 60 to 1000 km above the Earth (Campbell 2003 [9]) containing the largest concentration of free electrons. These ionospheric electric currents are caused by atmospheric disturbances, launched by seismic oscillations of the Earth's surface or the tsunami wavefield as inputs, which propagate upward into the ionosphere. These mechanisms are denominated litosphere-atmosphere-ionosphere (LAI) (Klausner et al. 2017 [28]) and tsunami-atmosphere-ionosphere (TAI) (Kherani et al. 2012 [25]) coupling, respectively. Recognizing which physical mechanism generates a ground-level magnetic

field perturbation represents a great challenge, since at each instant of time, a combination of signals with comparable orders of magnitude and coming from different layers of the Earth (ocean, ionosphere, magnetosphere, etc.) can contribute to an observation at a point (Campbell 2003 [9]). This challenge reveals itself in some discrepancies between existing studies regarding TGM signals.

During the 2010 Mw8.8 tsunami, generated after an earthquake in Chile on February 27, 2010 at 06:34 UTC, a periodic signal of 1 nT in the vertical component of the geomagnetic field was captured by the Easter Island Observatory (code IPM, according to the geomagnetic observatory network INTERMAGNET) (Manoj et al. 2011 [38]), located at (27.17 S, 109.41 W) in Easter Island, Chile, about 3500 km west of Chilean coast. This perturbation was recorded when the tsunami waves passed around Easter Island. Comparing the measurement with a numerical model, Wang et al. (2015) [74] reported an oceanic origin of the electric currents generating the perturbation. On the other hand, Klausner et al. (2014) [29] analysed the IPM measurements using the wavelet transform, and associated the dominant periods in the power spectrum to a possible influence of the TAI mechanism. During the 2015 Mw8.2 Chile tsunami, produced after an earthquake in Chile on September 16, 2015 at 22:55 UTC, IPM also showed a magnetic disturbance of about 1 nT in the vertical component, coincident with the tsunami arrival time. Following a procedure similar to Klausner et al. (2014) [29], Klausner et al. (2016) [27] suggested the ionospheric origin, via TAI coupling, of the electric currents. In contrast to the 2010 event, there is a lack of studies with numerical models related to the 2015 Chilean tsunami.

In addition to tsunami detection, data from IPM could also be used to investigate

the presence of mesoscale eddies. These eddies dominate the ocean current variability in the first hundred of meters at periods of 30-90 days, and they can transport heat, nutrient and organisms toward and around Easter Island, which is located in the eastern boundary of the south Pacific anticyclonic subtropical gyre, characterized by a very low level of nutrients and a high degree of endemism (von Dassow and Collado-Fabbri 2014 [73]). The connection between the variability of physical and biological properties within the gyre occurs at several spatial and temporal scales that are not fully understood, and OGM signals recorded at IPM might represent a suitable starting point in this research area. One example of this physical-biological connection is that vertical mixing, Ekman pumping, and thermocline displacement are the main driving mechanisms for observed seasonal changes in chlorophyll concentration within the gyre (McClain et al. 2004 [39]).

After pondering of the discussed considerations, the goal of this thesis is to investigate the possible influence of oceanic processes in the geomagnetic data recorded at the Easter Island Observatory in two cases particularly relevant for Chile: tsunamis and ocean circulation. The methodology used to accomplish the objective involves to compare magnetic records from the Easter Island Observatory with modelled magnetic disturbances for three time periods: during the 2010 and 2015 Chilean earthquake-induced tsunamis, and during the 2011-2015 period. The computed magnetic fields are obtained by combining ocean velocities, from numerical tsunami simulations and satellite altimeter data, with the Biot-Savart law in a rectangular area around Easter Island.

The thesis is divided in the following sections: Theoretical Considerations, Met-

hodology, Results and Discussion, and Conclusions.

Chapter 2

THEORY

2.1. Electromagnetic equations and PM/TM modal representation

To study electromagnetic processes in the ocean, it is necessary to use a set of equations valid in a accelerating reference frame (the Earth), and that considers a material medium (the ocean) moving with a velocity relative to a rotating observer attached to the spinning Earth. Tyler and Mysak (1995) [70] derived such equations assuming that Earth's rotation and ocean velocities were much smaller than the speed of light:

$$\nabla \cdot \vec{B} = 0, \tag{2.1}$$

$$\nabla \times \vec{E} = -\partial_t \vec{B}, \tag{2.2}$$

$$\nabla \times \vec{B} = \mu\sigma_s(\vec{E} + \vec{u} \times \vec{B}), \tag{2.3}$$

in which $\vec{E}(x,y,z,t)$ and $\vec{B}(x,y,z,t)$ are the electric and magnetic fields, μ is the seawater permeability (assumed to be $\mu = \mu_0$, its value in the free space), σ_s is the seawater electrical conductivity, and $\vec{u}(x,y,z,t) \equiv (u,v,w)$ is the ocean velocity field, where u, v, and w are the velocity components along the X-, Y-, and Z-axes, respectively. In Eq. 2.3, the form of the source electric current density, $\sigma_s(\vec{E}+\vec{u}\times\vec{B})$, indicates that it has a component at right angles to both the water current and the magnetic field. The electric currents in the water are composed by the bulk motion of the salt ions, which migrate transverse to the flow direction under the driving influence of the electromagnetic force. Remaining sources (displacement current and charge advection) are neglected when compared with the conduction current in the right-hand side (RHS) of Eq. 2.3 (Sanford 1971 [54]).

The total electric field developed in the seawater, $\vec{E}$, is composed of both those attributable directly to electric charges, and Faraday fields, associated with the changing magnetic fields in Eq. 2.2. The total magnetic field, $\vec{B}$, is composed of a tiny, OGM perturbation, and a "steady"(slowly varying with respect to the perturbation) Earth's main magnetic field due to electric currents in the Earth's core. A convenient and more general representation of $\vec{E}$ and $\vec{B}$ was introduced by Price (1950) [51], simplified by Weaver (1971) [77], and applied to the induction in the ocean by Chave (1983) [10]. It is based in the fact that, by defining a direction along which the electrical conductivity σ varies, e.g., the vertical coordinate, $\vec{E}$ and $\vec{B}$ may be separated into two modes relative to this direction, each of which satisfies Eqs. 2.2-2.3 independently: the toroidal magnetic (TM) and poloidal magnetic (PM) modes. The PM mode is characterized by electric current loops flowing in horizontal planes encircling the vertical axis, whereas the TM mode consists of electric currents

flowing in vertical planes. For this thesis, an important feature of this modal representation is that the electric current distribution associated with the TM mode has zero magnetic field outside a conductor. Applied to this case, the TM mode can only be detected inside the oceans, since it vanishes at the ocean surface, while the PM component reaches stations on land and at low-Earth-orbiting satellites.

Decomposing the total magnetic field $\vec{B} = \vec{b} + \vec{F}$ (with $\left|\vec{b}\right| \ll \left|\vec{F}\right|$) into the OGM part, $\vec{b}$, and the Earth's main magnetic field, $\vec{F}$, and following the PM/TM approach, Chave (1983) [10] expressed the magnetic field, $\vec{B}$, and the source electric current density, $\vec{J^0} = \sigma_s(\vec{u} \times \vec{F})$[1], in terms of scalar functions, as (the time dependence of all variables is taken to be proportional to $e^{-i\omega t}$):

$$\vec{B} = \nabla \times \nabla \times (\Psi \hat{z}) + \nabla \times (\Pi \hat{z}), \tag{2.4}$$

$$\vec{J^0} = J_z^0 \hat{z} + \nabla_h T + \nabla \times (\Upsilon \hat{z}), \tag{2.5}$$

where J_z^0 is the vertical source current, the subscript h refers to the horizontal components, the terms Π and T are related to the TM mode, the terms Ψ and Υ are related to the PM mode via the differential equation:

$$\nabla^2 \Psi - \mu\sigma\partial_t \Psi = -\mu\Upsilon, \tag{2.6}$$

[1]Lorentz body forces, i.e., $\vec{J^0} \times \vec{F}$, are negligible small when compared to dominant driving forces in the ocean, such as Coriolis and pressure gradient forces (Tyler 2006 [66]).

and Υ is solution of the Poisson equation:

$$\nabla_h^2 \Upsilon = -(\nabla \times \vec{J^0}) \cdot \hat{z}. \tag{2.7}$$

Combining Eq. 2.7 with $\vec{J^0} = \sigma_s(\vec{u} \times \vec{F})$, the electric current function related to the PM mode becomes:

$$\nabla_h^2 \Upsilon = \sigma_s(\vec{u}_h \cdot \nabla_h + \nabla_h \cdot \vec{u}_h)F_z - \sigma(\vec{F_h} \cdot \nabla_h + \nabla_h \cdot \vec{F_h})w, \tag{2.8}$$

according to the more complete solution of Chave (1989) [11]. We see that the PM mode is produced by coupling of the following terms in the RHS of Eq. 2.8:

1. Horizontal velocities with lateral variations of the vertical geomagnetic field.
2. Horizontally divergent part of the horizontal velocities with the vertical geomagnetic field.
3. Horizontal geomagnetic field with lateral variations of the vertical velocity.
4. Horizontally divergent part of the horizontal geomagnetic field with the vertical velocity.

2.2. Oceanic processes

Oceanic phenomena occur on a wide variety of scales in both time and space (Cushman-Roisin and Beckers 2011 [14], see their Fig. 1.7). In this thesis, magnetic perturbations induced by two of them, of very different temporal scales, will be investigated: tsunamis and meso-/large-scale circulation.

2.2.1. Tsunamis

Usually, tsunami waves produced by seismic motions of the seafloor have very long wavelenghts (λ), with orders of magnitude comparable to the horizontal dimension of their source (L), e.g., $\lambda \sim \ L \sim 100$ km. In addition, the typical depth of the ocean is $H \sim 4$ km. Therefore, this depth is significant smaller than the wavelength, i.e., $H/\lambda \ll 1$, and the shallow-water (or long-wave) theory is a suitable description for the main stages of a tsunami: generation of the wave, its propagation in open ocean, and its interaction with the coast (Levin and Nosov 2016 [34]).

According to the shallow-water theory, the vertical velocity, w, is much smaller than the horizontal velocities, u and v. Therefore, the latter are depth-independent and an initial three-dimensional hydrodynamic problem reduces to a two-dimensional problem by integrating the shallow-water equations along the vertical coordinate (Kundu and Cohen 2008 [31]; Levin and Nosov 2016 [34]). Expressed in total fluxes, the non-linear equations of the shallow-water theory which describe conservation of momentum and mass with account of the bottom friction and the Coriolis force, are:

$$\partial_t M + \partial_x \left(\frac{M^2}{D} \right) + \partial_y \left(\frac{MN}{D} \right) = -gD\partial_x \xi + fN - \frac{C_B M \sqrt{M^2 + N^2}}{D^2}, \tag{2.9}$$

$$\partial_t N + \partial_x \left(\frac{MN}{D} \right) + \partial_y \left(\frac{N^2}{D} \right) = -gD\partial_y \xi - fM - \frac{C_B N \sqrt{M^2 + N^2}}{D^2}, \tag{2.10}$$

$$\partial_t \xi + \partial_x M + \partial_y N = -\partial_t \eta, \tag{2.11}$$

in which (M,N) denote the volume fluxes in X (West-East) and Y (South-North) directions, respectively. (M,N) are product of velocities and the thickness of the water column, $D(x, y, t) = \xi(x, y, t) + H(x, y)$, where ξ is the displacement of the free surface of water from its equilibrium position and $H(x, y)$ is the water depth, g is the gravitational acceleration, $f = 2\Omega \sin \varphi$ represents the Coriolis force coefficient due to the Earth's rotation, Ω is the angular velocity of the Earth, φ is the latitude, C_B is a dimensionless empirical coefficient, which is usually set to 0.0025, and $\eta(x, y, t)$ is the dynamic deformation of the bottom.

A review including the progress in numerical simulations of TGM fields, i.e., models based on Eqs. 2.1-2.3 and Eqs. 2.9-2.11, was presented by Minami (2017) [42]. A remarkable study also is that of Kherani et al. (2012) [25], who used numerical solutions of Eqs. 2.9-2.11 as inputs in a TAI-coupled simulation model, the latter including a more complete version of Eqs. 2.1-2.3 to describe hydromagnetic fluctuations in the ionosphere during the 2011 Tohoku-Oki tsunami. For the same event, Minami and Toh (2013) [44] and Minami et al. 2017 [45] developed simulation codes, based on the same equations, to study the motional induction by the ocean. An application of the modelling of TGM variations is that of Kawashima and Toh (2016) [24], who infered tsunami properties, e.g., the fault slip model, of the causative 2007 Kuril earthquake.

2.2.2. Ocean circulation

The circulation in midlatitude oceans is driven mainly by atmospheric wind systems blowing along the sea surface. The effect of the wind stress is confined to the surface Ekman layer set up just below. The wind-stress curl generates, in turn, a ver-

tical velocity through the flow, outside of the Ekman layer (Cushman-Roisin 1994 [13]). If the ocean flow extends over a sufficient wide area, the variation of the Coriolis force coefficient with latitude is not negliglible, and the beta-plane approximation is necessary. This beta effect is related to the geostrophic flow in the interior of the ocean. The governing equations of the flow are (Cushman-Roisin and Beckers 2011 [14]):

$$-(f_0 + \beta_0 y)v = -\frac{1}{\rho_0}\partial_x p, \tag{2.12}$$

$$(f_0 + \beta_0 y)u = -\frac{1}{\rho_0}\partial_y p, \tag{2.13}$$

$$0 = -\frac{1}{\rho_0}\partial_z p, \tag{2.14}$$

$$\partial_x u + \partial_y v + \partial_z w = 0, \tag{2.15}$$

in which $f_0 = 2\Omega \sin\varphi_0$ is a reference Coriolis parameter, $\beta_0 = 2(\Omega/a)\cos\varphi_0$ is the beta parameter, a is the earth's radius (6371 km), ρ_0 is the reference density of the ocean, and p is the pressure.

Other large-scale, low frequency, phenomena at midlatitudes zones are the planetary waves, in which the steady geostrophic flows develop a slow time evolution

(Cushman-Roisin 1994 [13]):

$$\partial_t u - (f_0 + \beta_0 y)v = -g\partial_x \xi, \tag{2.16}$$

$$\partial_t u + (f_0 + \beta_0 y)u = -g\partial_y \xi, \tag{2.17}$$

$$\partial_t \xi + H\left(\partial_x u + \partial_y v\right) = 0. \tag{2.18}$$

In Eqs. 2.16-2.18, the time derivatives and β_0 terms are the small perturbations which govern the wave evolution.

OGM signals related to these large-scale movements of water have been investigated theoretically, using the PM/TM modal representation, by Chave and Luther (1990) [12]. Tyler and Mysak (1995) [71] combined idealized currents, e.g., sheared plane-parallel flows and gyres, with the magnetic induction equation (Eq. 4.3). Using both satellite altimeter data and datasets from the global, 3-D Ocean Model for Circulation and Tides (OMCT) as inputs for a 3-D solver of Eqs. 2.1-2.3, Saynisch et al. (2018) [55] also investigated ocean circulation's magnetic signals.

2.3. A magnetostatic model for the ocean motional induction

In Section 2.1, factors which produce PM fields were introduced (see Eq. 2.8). In order to consider the first and fourth terms, $\sigma_s \vec{u}_h \cdot \nabla_h F_z$ and $\sigma_s \nabla_h \cdot \vec{F}_h w$, in a realistic

case, geomagnetic field values for every grid cell in the study area and a subsequent finite difference scheme to calculate the horizontal derivatives are required[2]. For convenience, and since in this thesis the seawater motion is restricted to a local scale, static values (both vertically and horizontally constant) of geomagnetic fields are taken, and the first and fourth terms in the RHS of Eq. 2.8 play no role, therefore:

$$\nabla_h^2 \Upsilon = \sigma_s F_z \nabla_h \cdot \vec{u}_h - \sigma_s \vec{F}_h \cdot \nabla_h w, \tag{2.19}$$

and, in this case, the source mechanisms for the PM mode are the interactions of both the vertical component of the geomagnetic field with the horizontally divergent part of the horizontal velocity field, and horizontal geomagnetic field with lateral variations of the vertical velocity. A further simplification can be made since the numerical tsunami simulations and satellite altimeter data used in this research provide only horizontal velocities. Therefore, the second term in Eq. 2.19 may be neglected relative to the first, becoming:

$$\nabla_h^2 \Upsilon = \sigma_s F_z \nabla_h \cdot \vec{u}_h. \tag{2.20}$$

Thus, the only source mechanism for the PM mode considered in this work is the coupling of the vertical component of the geomagnetic field with the horizontally divergent part of the ocean velocity field. The source electric current density in its

[2]An utility program for providing geomagnetic field values for any grid location is GEOMAG, which is available online (`https://www.ngdc.noaa.gov/geomag/calculators/magcalc.shtml#igrfgrid`). The field values are based on the International Geomagnetic Reference Field (IGRF) model, which is a series of mathematical models of the Earth's magnetic field and its annual rate of change (Campbell 2003 [9])

explicit form is:

$$\vec{J^0} = \sigma_s(vF_z\hat{x} - uF_z\hat{y}). \tag{2.21}$$

Once this driving electric current is obtained, the resulting magnetic fields could be calculated by using Eqs. 2.1-2.3. However, since the best known hypothesis for generating the geomagnetic field, $\vec{F}$, is that the Earth's liquid outer core maintains an electric current as a "self-excited dynamo", it is convenient to noting that outside of this core $\vec{F}$ is irrotational (Campbell 2003 [9]) and the left-hand side (LHS) of Eq. 2.3 is replaced by $\nabla \times \vec{b}$. Further, since the calculation of the Faraday-induced electric field in the LHS of Eq. 2.2 would involve to solve time derivatives while working with bathymetry and velocity data, the self-induction term $\partial_t \vec{b}$ is neglected. For the same reason, the electrostatic field due to electric charges is neither considered.

With the aforementioned assumptions, a magnetostatic model to study the influence in the Earth's magnetic field of oceanic processes around Easter Island is proposed. The model is based on the Biot-Savart law. This law allows to calculate a net induced magnetic field $\vec{B}$ at an observation point $\vec{x}$ when the electric current distribution is a known function of position (Griffiths 2013 [18]):

$$\vec{B}(\vec{x}) = \frac{\mu_0}{4\pi} \int_{\mathcal{C}} \frac{\vec{I}(\vec{x}') \times (\vec{x} - \vec{x}')}{|\vec{x} - \vec{x}'|^3} d\vec{x}', \tag{2.22}$$

where by the superposition principle, the contributions of differential elements of a wire, located at $\vec{x}'$ and carrying electric currents $\vec{I}(\vec{x}')$ which generate small fields $d\vec{B}(\vec{x})$, are added up (Fig. 2.1).

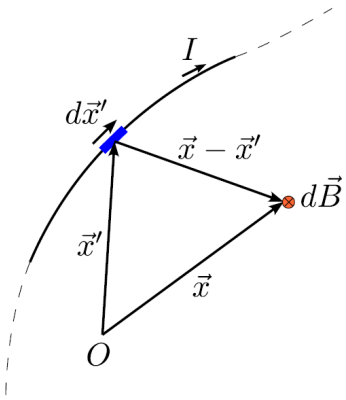

Figure 2.1: Illustration of the Biot-Savart law. (From Rubilar 2016 [53].)

Chapter 3

METHODOLOGY

3.1. Oceanographic data

The oceanic currents associated with the 2010 and 2015 Chilean tsunamis were computed using the Fortran-based freeware COrnell Multi-grid COupled Tsunami model (COMCOT), version 1.7 (Wang 2009 [76]). COMCOT v1.7 adopts leap-frog finite difference schemes to solve linear shallow water (LSW) and nonlinear shallow water (NSW) equations in both spherical and cartesian coordinates (Eqs. 2.9-2.11). In the leap-frog method, the evaluation of water surface elevation, ξ, and volume fluxes, M and N, is staggered in time and space. For each time step of an entire tsunami simulation, the aforementioned parameters are output in data files at all the grid points.

To fulfill the need for tsunami simulations in different scales, COMCOT v1.7 uses a nested grid system. A nested grid configuration means that in a region of one grid size, one or more regions with higher resolutions and time step sizes can be imbedded. Either the LSW or NSW equations with either spherical or cartesian coordinate system can be assigned to a specific sub-level region, and these layers exchange infor-

mation regarding water surface elevations and volume flux components. The nested grid system allows to obtain detailed information in coastal regions, where finer grids are required to resolve wave profiles, since the length of tsunami waves will become much smaller than in deep ocean.

To perform the tsunami numerical calculations for both events, heterogeneous fault models of the seafloor deformation were used as initial conditions. The seafloor deformation data were constructed and validated in Koper et al. (2012) [30] for the 2010 tsunami, and constructed in Benavente et al. (2016) [6] and validated in Calisto et al. (2016) [8] for the 2015 event. 18 h of tsunami propagation were simulated for both events. The nested grid system was configured as follows: the first-level grid, with a resolution of 2.16 arcmin, is common for all locations (Fig. 3.1, left). Second-(black rectangle in Fig. 3.1, left) and third-(Fig. 3.1, right) level grids, with respective resolutions of 0.27 and 0.054 arcmin, were constructed around Easter Island. In order to validate the numerical models, a comparison between modelled and measured sea surface elevations was performed by constructing second-, third- and fourth-level grids with 0.54, 0.108 and 0.018 arcmin, respectively, for three locations along the Chilean coast that have high resolution bathymetric and tide gauge data available (black squares in Fig. 3.1, left). Four DART buoy locations were also used (orange diamonds in Fig. 3.1, left). Bathymetric data were kindly provided by I. Calisto during the research period. More details and results regarding the validation process can be found in Torres et al. (2019) [64].

For investigating OGM signals in the period between 15 May 2011 to 15 September 2015, daily water velocities with a resolution of 0.25° latitude by 0.25° longitude

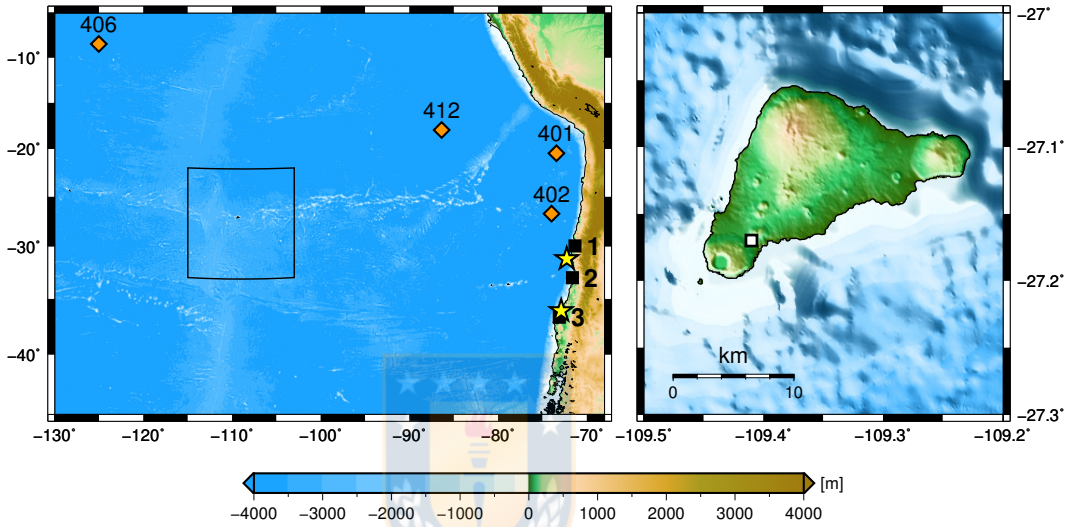

Figure 3.1: Left: The first-level bathymetric grid, showing 2015 and 2010 epicenters (north and south yellow stars, respectively); the positions of DART buoys 32401, 32402, 32406 and 32412 (orange diamonds); and the three coastal locations from north to south, Coquimbo, Valparaíso and Talcahuano (black squares). The black rectangle indicates the position of the second-level grid around Easter Island. Right: The third-level grid around Easter Island, showing the location of the Easter Island Observatory (white square). Abscissa and ordinate are longitude and latitude, respectively. (From Torres et al. 2019 [64].)

were obtained using satellite altimeter data from the Copernicus Marine and Environment Monitoring Service (CMEMS) (`http://www.marine.copernicus.eu`). A grid region around Easter Island, defined by the coordinates of its south-west corner (41.875 S, 124.875 W) and north-east corner (12.125 S, 95.125 W), was considered in this case. Displacements of parcels of water, each one degree away from Easter Island and starting from eastward (E), westward (W), northward (N) and southward (S) positions (Fig. 3.2), illustrate the fact that the island is located within an anticlockwise gyre. These progressive vector diagrams were constructed from the altimeter data for currents measured at the four locations.

3.2. Implementation of the magnetic model

The appropiate form of Eq. 2.22 for its application in this thesis is:

$$b_z(\vec{r}) = \frac{\mu_0}{4\pi} \sum \frac{\Delta I_x(\vec{x}')(y-y')\Delta x' - \Delta I_y(\vec{x}')(x-x')\Delta y'}{((x-x')^2+(y-y')^2+(z-z')^2)^{3/2}}, \tag{3.1}$$

where the X- and Y- components of the source electric currents, $\Delta I_x(\vec{x}')$ and $\Delta I_y(\vec{x}')$, as function of its location $\vec{x}'$ at each grid cell of the rectangular area around Easter Island, are:

$$\begin{aligned} \Delta I_x(\vec{x}') &= \sigma_s N(\vec{x}') F_z \Delta y', \\ \Delta I_y(\vec{x}') &= -\sigma_s M(\vec{x}') F_z \Delta x'. \end{aligned} \tag{3.2}$$

In Eqs. 3.1-3.2, $\Delta x'$ and $\Delta y'$ are widths of each grid cell in the X- and Y- directions, respectively. Eqs. 3.2 are computed using either the set of water flux values

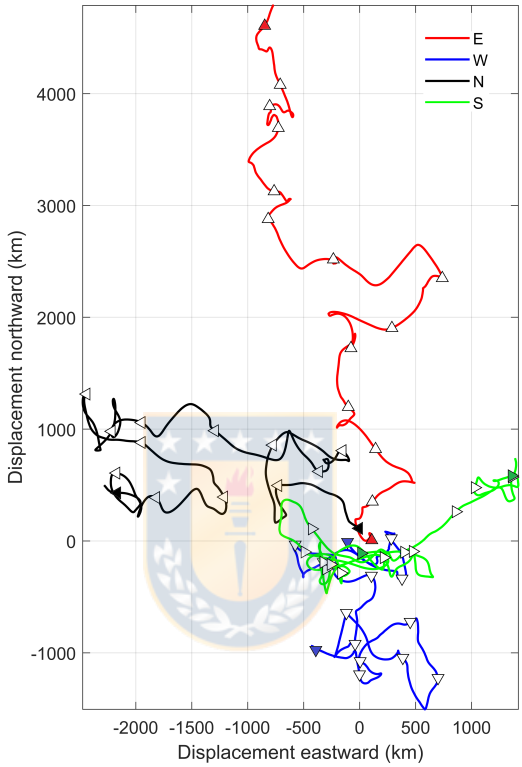

Figure 3.2: Time-integrated horizontal displacements of parcels of water, each starting from eastward (E), westward (W), northward (N) and southward (S) positions, one degree away from Easter Island (at the origin). These initial locations are represented by red, blue, black and green triangles, respectively, around the island. Markers (white triangles) are displayed every 120 data points. Displacements and final positions are represented with the same colours as the starting points.

$(M(\vec{x}'),N(\vec{x}'))$ obtained from the tsunami calculations or the altimeter data. In the last case, data are a suitable representation of the oceanic currents only in the first 300-500 m, approx., and an uniform water depth of 400 m was considered in the study area, instead of the entire water column as for the tsunami cases. The third term in the denominator of Eq. 3.1, $(z - z')$, is actually not considered since the elevation of IPM (83 m) is much smaller than the horizontal distances, $(x - x')$ and $(y - y')$, between the station and the grid cells, and the study area is assumed to be a thin (with no Z-dependence), long wire composed of segments (Eq. 3.2) carrying electric currents. Values of F_z were calculated using a mean of the original measurements at IPM. For the 2011-2015 period and 2010 and 2015 tsunamis, $F_z = 19500$ nT, $F_z = 19611$ nT and $F_z = 19439$ nT were obtained, respectively. Since the electric current distribution changes with time as waves or currents propagate in the ocean, the time series of the OGM fields were obtained by evaluating Eq. 3.1 for each time step.

The value of σ_s is temperature- and salinity-dependent. For example, at $T = 15$ °C and $s = 35$ psu, σ_s =4.29 S/m, approx. Moreover, it is a function of the mass, charge, number of charges per unit volume, and collision time over all ionic species, both negative and positive, present in the seawater (Apel 1999 [3]). In order to consider a realistic distribution of σ_s, circulation models which solve equations for heat and salt, e.g., OMCT, may be used. For simplicity, an homogeneous conductivity is assumed is this work. Since Wang et al. (2015) [74] used $\sigma_s = 4$ S/m to investigate the magnetic anomaly generated at Easter Island during the 2010 event, this value was chosen in each situation. Moreover, by considering other values of conductivity, e.g., σ_s =3 - 3.5 S/m, in both tsunami simulations, negligible differences between the

TGM signals were obtained (results not shown).

Summarizing, the methodology for computing the modelled fields involved four main steps:

1. For the tsunami events and the period 2011-2015, obtaining either the seawater volume fluxes from the numerical tsunami calculations or the seawater velocities from satellite altimeter data, respectively.

2. Computation of time series of ocean-generated electric currents within a rectangular area around Easter Island using eqs. 3.2.

3. Using the Biot-Savart law (eq. 3.1), computation of the net OGM fields at IPM by adding up all the magnetic fields arising from each electric current element over the simulation space.

4. Comparison between the computed time series and magnetic records observed at IPM.

3.3. Magnetic measurements and data processing

The operation of the IPM station (white square in Fig. 3.1, right), belonging to the International Real-Time Magnetic Observatory Network (INTERMAGNET) program (`https://www.intermagnet.org/imos/imos-list/imos-details-eng.php?iaga_code=IPM`), is supported by Dirección Meteorológica de Chile and Institut de Physique du Globe de Paris, France. The observatory has a magnetometer with a 0.1 nT resolution, and provides time series of three magnetic components quoted with respect to a local right-handed geographical tangent plane: X (northward), Y

(eastward), and Z (downward), at time intervals of 1 min. In this work, however, the coordinate system used by COMCOT v1.7 (X-, Y-, and Z- components in eastward, northward and upward directions, respectively) was followed. After downloading the data from the webpage, a cubic spline data interpolation was carried out when the records were corrupted or presented gaps.

In the case of the 2011-2015 period, the original sample rate of the magnetic records was reduced in order to obtain daily data. Since rotary spectra (Fig. 3.3) for five years of daily currents measured at the same locations of Fig. 3.2 show peaks around 90-120 and 30-40 days, approx., the analysis of the magnetic signals was focused on the 33- to 135- days band. With the lower time scale limit, a possible influence of the luni-solar monthly harmonic (31.8-day period) of the tidal force (Le-Blond and Mysak 1978 [33]) was prevented. In addition, relevant temporal scales for ocean-related climate studies at midlatitude zones, such as the Easter Island Province, start at around one month (Hasselmann 1982 [20]; Apel 1999 [3]).

In order to find common period ranges where magnetic data and the model were in agreement, wavelet power spectra were calculated for both signals according to the analysis guide of Torrence and Compo (1998) [63]. A Morlet wavelet (with $\omega_0 = 6$) was chosen, since it provides a good balance between time and frequency localization (Grinsted et al. 2004 [19]). Then, normalized, zero-lagged cross-correlations between horizontal slices taken through each wavelet power spectrum, which represent power time series in a certain period, were obtained. This procedure resembles, in a certain way, the method described in section 5b of Torrence and Compo (1998) [63]. Extreme values at 52 and 43 days were found (Fig. 3.4). Therefore, a reconstruction around

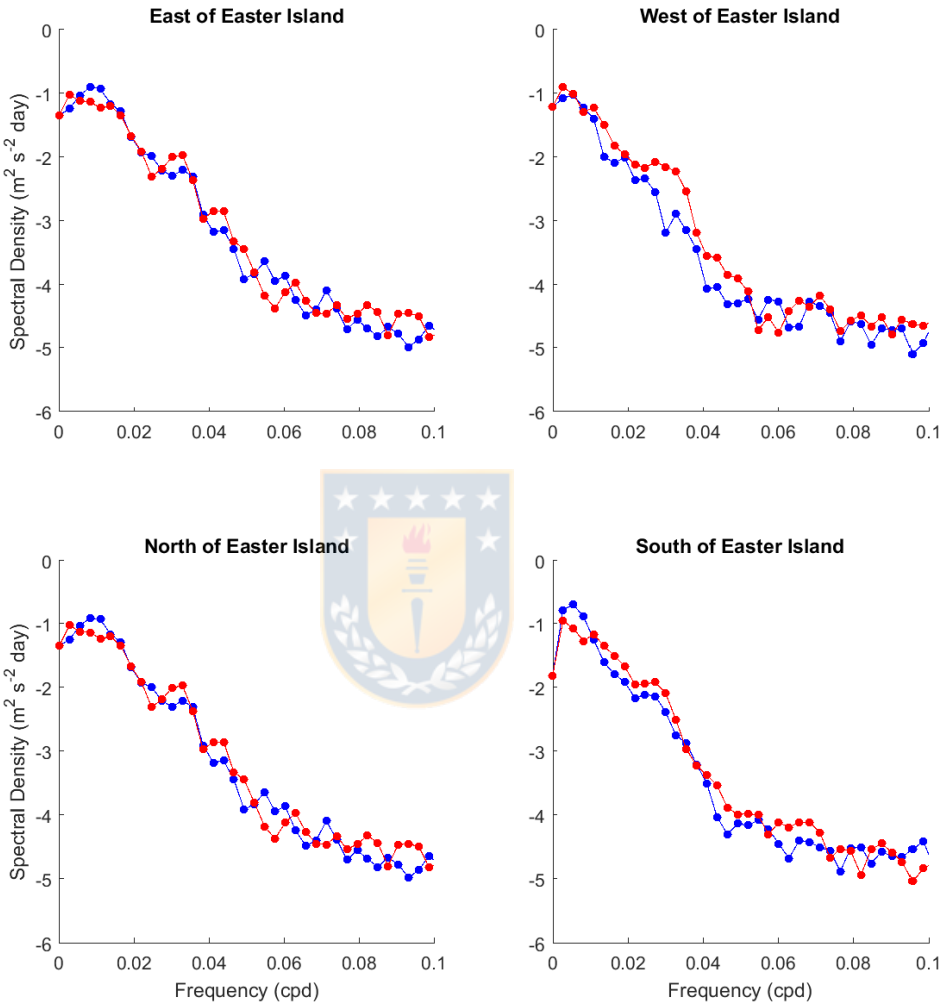

Figure 3.3: Clockwise (blue) and counterclockwise (red) rotary spectra for five years of velocity data for daily currents measured at four locations, each one degree away from Easter Island, in eastward (E), westward (W), northward (N) and southward (S) directions.

these periods of both the modelled OGM and magnetometer signals was conducted. Following the procedure described in section 5.5.1 of Emery and Thomson (2001) [15], the reconstruction was done by using a harmonic analysis, in which the frequencies of interest are specified by the user and a least-squares method is applied in order to solve for their various amplitudes and phases. The frequencies were obtained from the spectra of the time series, in the entire study period, which were in turn computed using the fast Fourier transform algorithm.

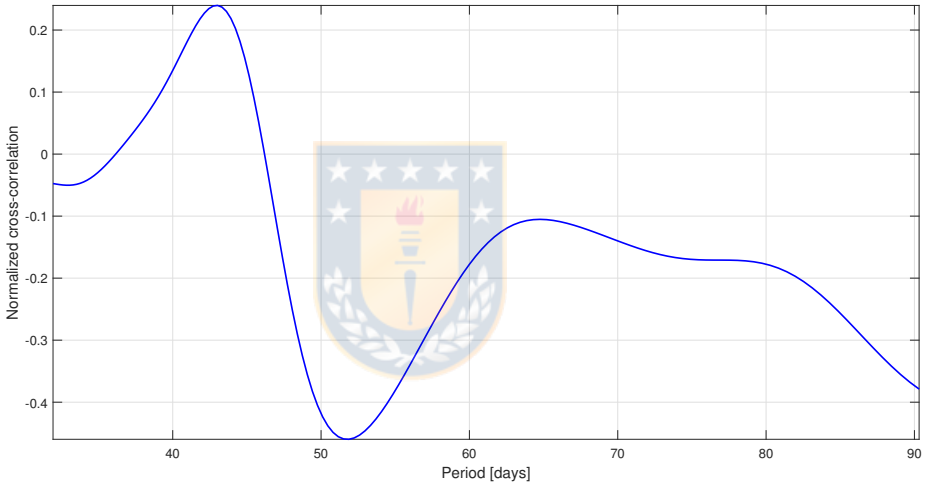

Figure 3.4: Normalized cross-correlations between power time series, of each wavelet power spectrum, versus periods.

In the tsunami cases, the modelled TGM and magnetometer signals were high-pass filtered in order to focus the analysis only on the periods of the tsunami waves instead of those related to after-tsunami processes, such as resonance phenomena and edge waves along coastlines, which depend mainly on the shape of the island, the contours of the surrounding sea bed, the length of the coastline, among others (Longuet-Higgins 1967 [35]; Yamazaki and Cheung 2011 [78]). Wavelet-filtered time series were obtained by adding up the real part of the wavelet transform of each

signal over the corresponding subset of periods, following the procedure described in section 3i of Torrence and Compo (1998) [63]. A Morlet wavelet (with $\omega_0 = 6$) and a cutoff period of 25 min were chosen for the filtering process. The choice of this cutoff period was based on the period content, obtained from wavelet power spectra (lower panels in Figs. 3.5, 3.6), of time series (upper panels in Figs. 3.5, 3.6) from a virtual mareograph located 2.5 km from IPM. Spectra were calculated using 750-min series.

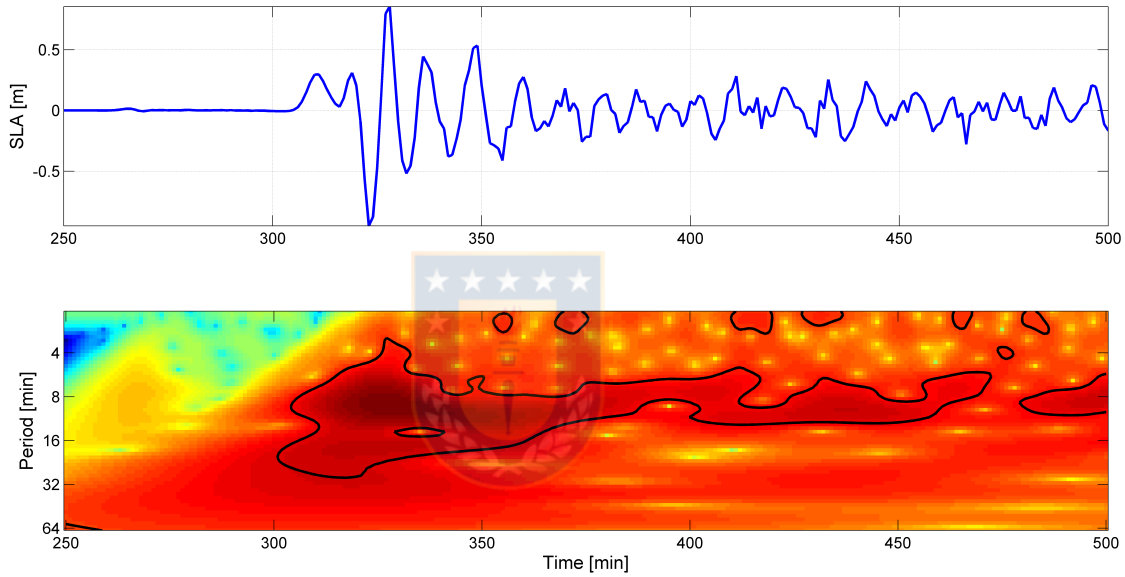

Figure 3.5: Sea level anomaly (SLA) (up) and its wavelet power spectrum (bottom) at (27.188 S, 109.391 W) for the 2010 Chile tsunami. Areas of stronger power are shown in dark red color on a plot of time (horizontal) and period (vertical). Time is measured relative to the earthquake origin time.

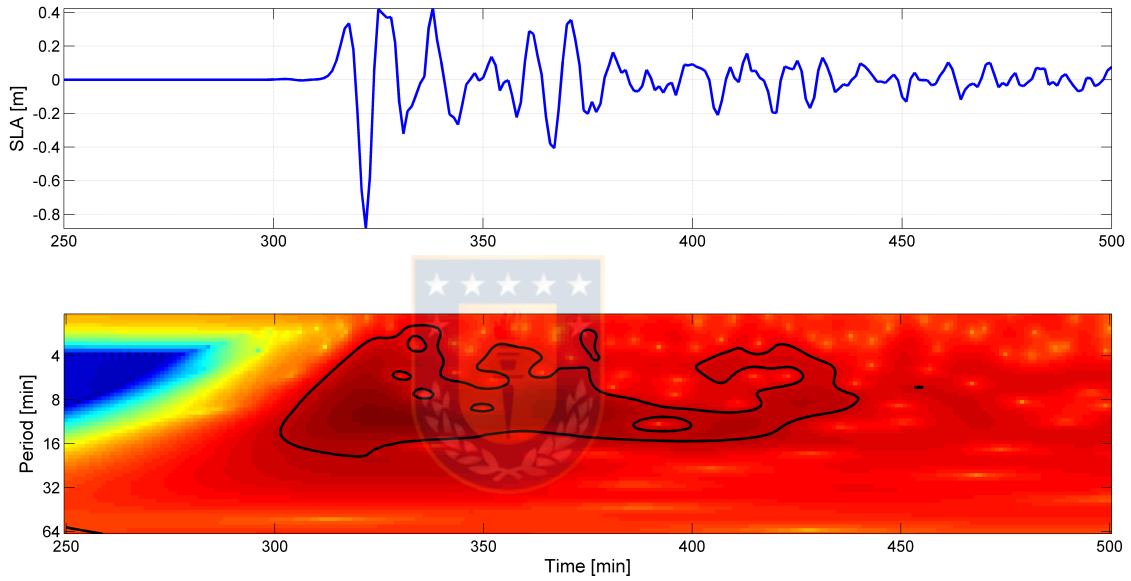

Figure 3.6: Sea level anomaly (SLA) (up) and its wavelet power spectrum (bottom) at (27.188 S, 109.391 W) for the 2015 Chile tsunami. Areas of stronger power are shown in dark red color on a plot of time (horizontal) and period (vertical). Time is measured relative to the earthquake origin time.

Chapter 4

RESULTS AND DISCUSSION

4.1. Tsunamis

4.1.1. 2010 Chilean tsunami

The observed and computed magnetic field variations at IPM for the 2010 event are shown in Fig. 4.2. A clear signal displaying seven peaks between 320 and 390 min after the earthquake was recorded at the observatory, coincident with the passing of the tsunami wave train around Easter Island (Fig. 4.1). The numerical model can predict magnetic perturbations, reproducing the shape and timing of observed peaks between 325 and 360 min, despite some disagreements in amplitude. Between 250 and 300 min, the model shows an initial oscillation and a trough, and does not reproduce the measurement. The amplitude is well represented between 400 and 600 min, although the timing agrees only partially in both waveforms.

4.1.2. 2015 Chilean tsunami

The temporal variations in the observed and computed magnetic field at IPM for the 2015 event are shown in Fig 4.4. A signal displaying several distinctive peaks,

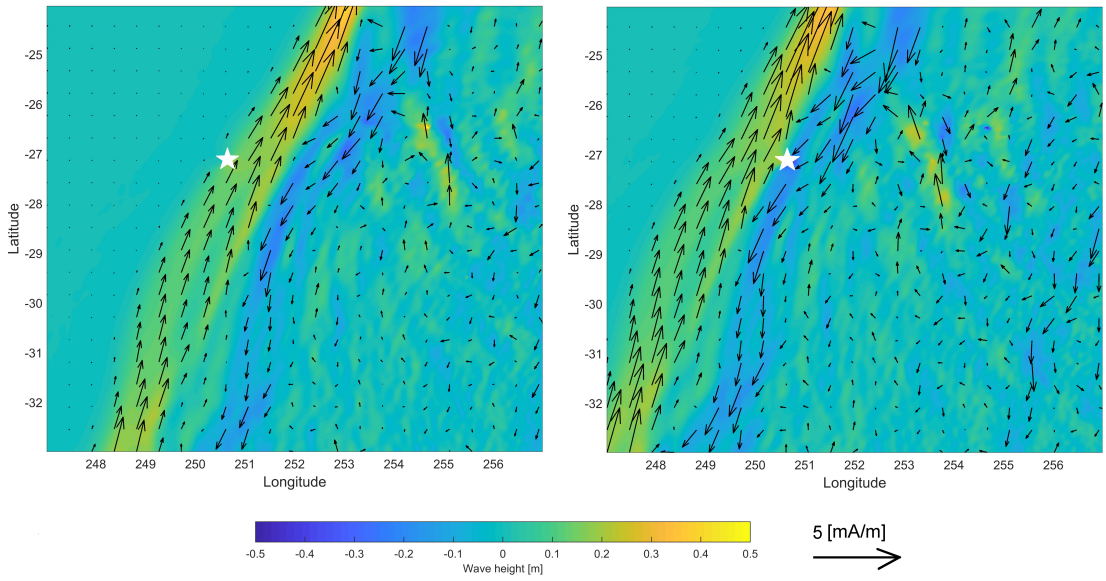

Figure 4.1: Simulated tsunami wave height (color images) and induced electric currents (black arrows) around Easter Island (white star) for the 2010 Chile tsunami at 308 min (left) and 320 min (right), instants of time when the model (red line in Fig. 4.2) predicts the first peak and trough. Time is measured relative to the earthquake origin time. (From Torres et al. 2019 [64].)

against a background oscillation, was recorded at IPM between 325 and 390 min, coincident with the passing of the tsunami around Easter Island (Fig. 4.3). Similar to the 2010 event, the model can reproduce magnetic perturbations. From 320 to 340 min there is a phase shift of about 5 min between calculated and observed signals, which vanishes at 350 min. With a hypothetical correction of this time lag, the resulting model and measurement would be similar, despite some differences in amplitude values, especially at the leading part of the signals. From 375 min, amplitudes are similar in both waveforms, but the model predicts shapes not present in the measurement.

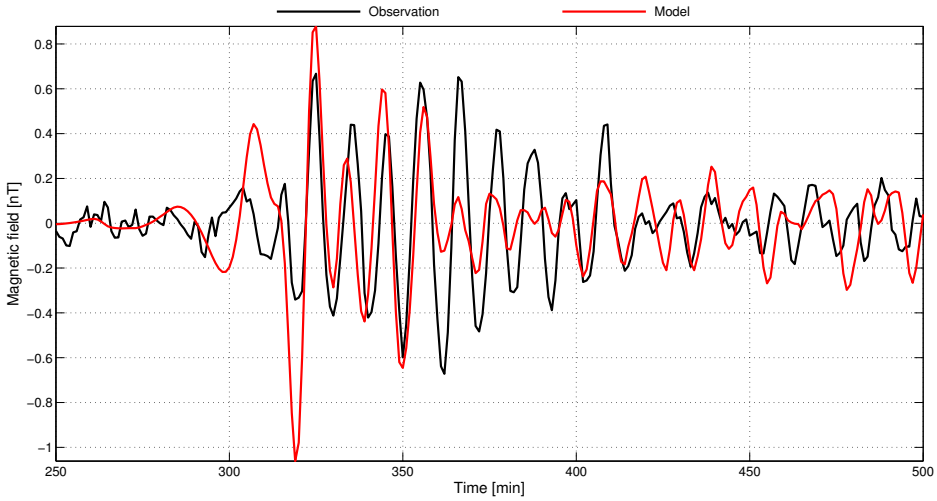

Figure 4.2: Comparison between the high-pass filtered magnetic field measurement (black line) and calculated TGM field (red line) at IPM for the 2010 Chile tsunami. Time is measured relative to the earthquake origin time. (From Torres et al. 2019 [64].)

Although earthquake-induced tsunami waves are long compared to the ocean depth, possible wave dispersive effects may become important by considering the integrated effect of the wavelength, the water depth during propagation, and the propagation distance or time. Moreover, dispersive waves interacting with the natural frequencies of the continental shelves, bays or harbors tend more often to generate constructive interference as compared to long waves (Horrillo et al. 2006 [21]). Based on theoretical threshold values proposed by Glimsdal et al. (2013) [16], Poupardin et al. (2018) [50] suggested to consider dispersion for distances larger than 1000 and 6500 km from the 2015 and 2010 tsunami sources, respectively. Considering the distance between Easter Island and the Chilean coast, the irrelevance of the dispersion in the 2010 event was expected, different from the 2015 tsunami, whose wave train was expected to be affected by dispersion at least in its trailing part. In this case,

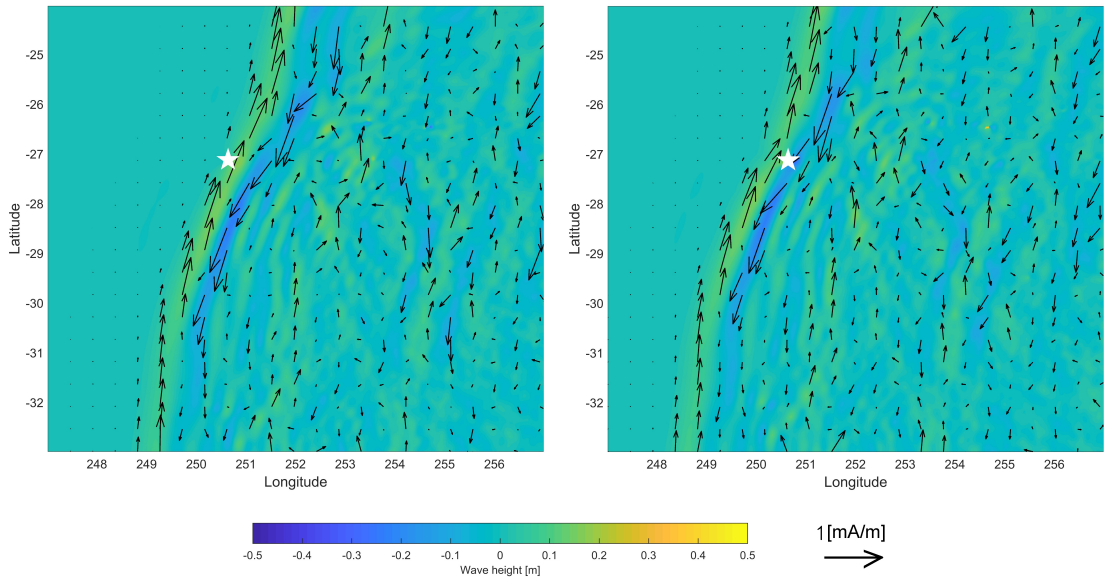

Figure 4.3: Simulated tsunami wave height (color images) and induced electric currents (black arrows) around Easter Island (white star) for the 2015 Chile tsunami at 313 min (left) and 318 min (right), instants of time when the model (red line in Fig. 4.4) predicts the first peak and trough. Time is measured relative to the earthquake origin time. Note the different electric current values compared to those displayed in Fig. 4.1. (From Torres et al. 2019 [64].)

the time lag between the calculated and observed signals in Fig. 4.4 was initially attributed to the dispersion.

In order to verify whether the frequency dispersion of tsunami waves could produce observable manifestations in the magnetic measurements, calculations using a frequency dispersion-improved algorithm of COMCOT were conducted. However, no significant differences (especially in the wave front) to the original results were found (Figs. 4.5- 4.6). The leapfrog scheme employed by COMCOT to solve Eqs. 2.9-2.11 introduces numerical errors, which are used to mimic the physical dispersion (inhe-

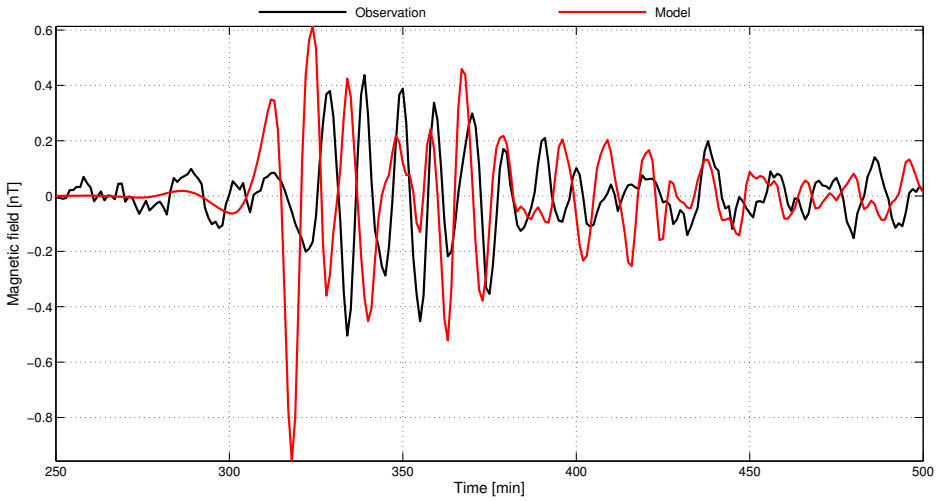

Figure 4.4: Comparison between the high-pass filtered magnetic field measurement (black line) and calculated TGM field (red line) at IPM for the 2015 Chile tsunami. Time is measured relative to the earthquake origin time. (From Torres et al. 2019 [64].)

rent to the Boussinesq equations) subject to an appropiate choice of grid and time step sizes (Wang 2009 [76]). Under this approach, the two-term expansion of the dispersion relation in terms of κH is satisfied:

$$c^2 \approx c_0^2 \left(1 - \frac{1}{3}(\kappa H)^2\right), \tag{4.1}$$

where c is the phase speed. The second term in the RHS of Eq. 4.1 represents frequency dispersion, since now the speed propagation of a wave component depends on its wavenumber, as opposite to the shallow-water theory, which only yields the unitary constant (Kundu and Cohen 2008 [31]).

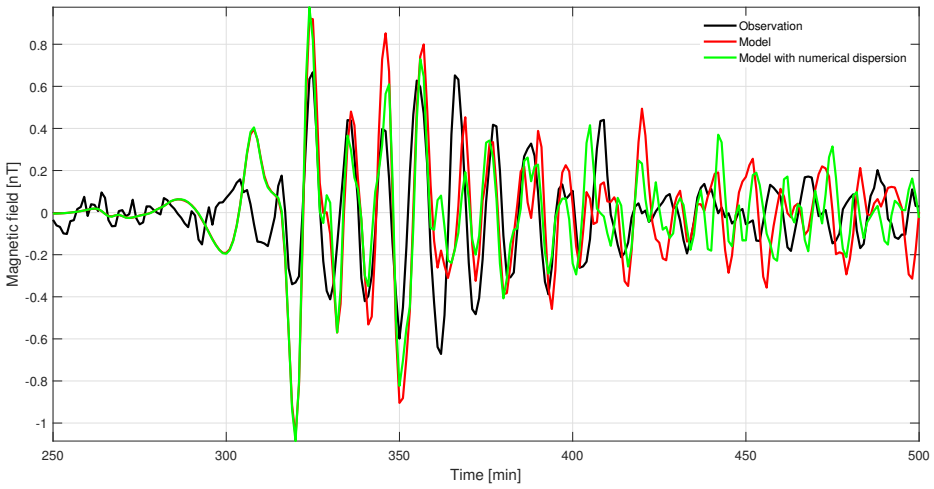

Figure 4.5: Comparison between the magnetic field measurement (black line), calculated TGM field (red line), and calculated TGM field using the numerical dispersion of COMCOT (green line) at IPM, for the 2010 Chile tsunami, considering a resolution of 1.08 arcmin for the second level grid around Easter Island. Time is measured relative to the earthquake origin time.

4.2. Meso- and large-scale marine currents

A comparison between the magnetic field measurement and calculated OGM field at IPM for the days 15 May 2011 to 15 September 2015, and their spectra, are shown in Figs. 4.7- 4.8, respectively. Spectra from Fig. 4.8 were calculated according to the procedure described in section 5a of Torrence and Compo (1998) [63]. Root-mean-square errors (Table 4.1) between observed and computed variations were calculated according to the values found in Fig. 3.4. Comparisons between signals for 33- to 135-, 33- to 48-, 33- to 38-, 33- to 39-, 39- to 48- and 39- to 47-day periods are shown in Figs. 4.9, 4.10, 4.11, 4.12, 4.13 and 4.14, respectively. In Fig. 4.10, the calculation

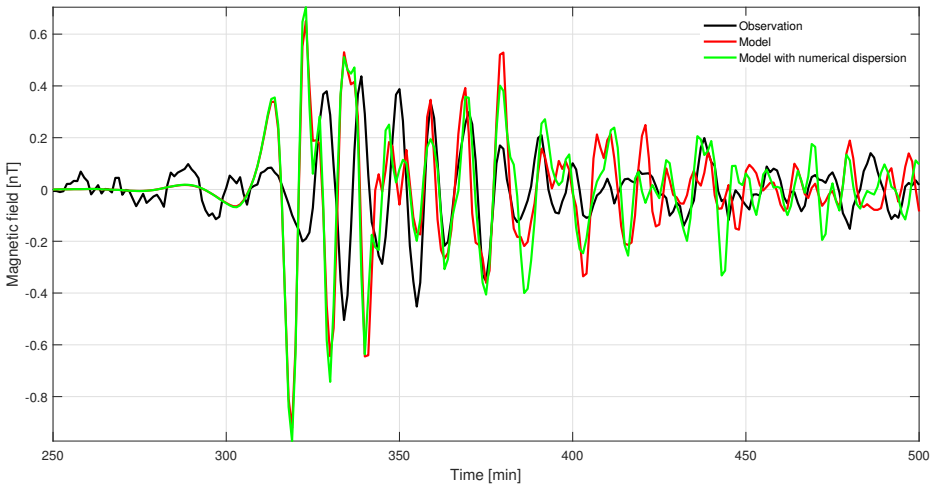

Figure 4.6: Comparison between the magnetic field measurement (black line), calculated TGM field (red line), and calculated TGM field using the numerical dispersion of COMCOT (green line) at IPM, for the 2015 Chile tsunami, considering a resolution of 1.08 arcmin for the second level grid around Easter Island. Time is measured relative to the earthquake origin time.

result shows a reasonable agreement in amplitude and time with the observation between days 790 and 940, in spite of a time lag of 3-4 days. In the rest of the time series, discrepancies become important, sometimes even showing a relation in antiphase. By lowering the upper limit of the periods range to 38 or 39 days (Figs. 4.11- 4.12), improvements in the comparison of observation and model are obtained. An extended length of time (days 600 to 900, approx.) shows similar values of amplitude for both the model and the data.

In the 39- to 48-day period band (Fig. 4.13), the model reproduces well the observation in the intervals 220-260 and 800-900 days, approx. By lowering the upper limit of the periods range to 47 days (Fig. 4.14), the length of time where the signals

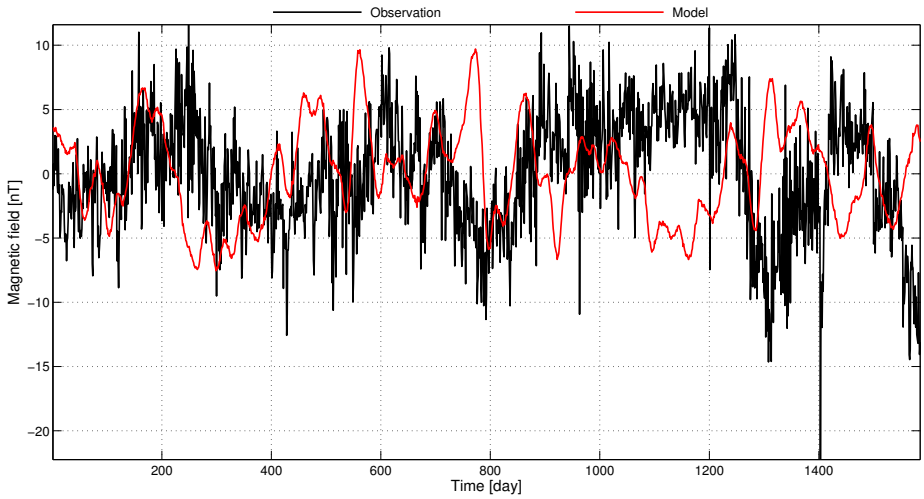

Figure 4.7: For the days 15 May 2011 to 15 September 2015, comparison between the magnetic field measurement (black line) and calculated OGM field (red line) at IPM. Time is measured relative to the starting date of the observations.

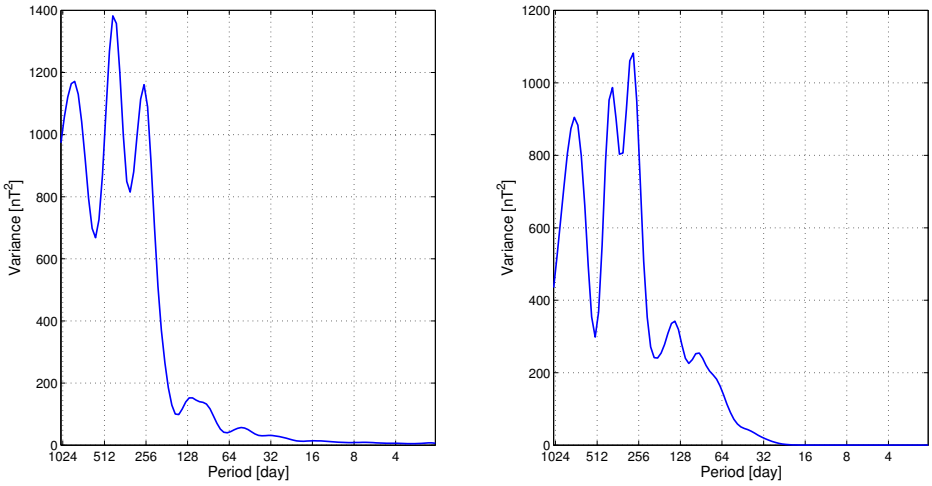

Figure 4.8: Global wavelet spectra for the magnetic field measurement (left) and calculated OGM field (right) at IPM in the period from 15 May 2011 to 15 September 2015.

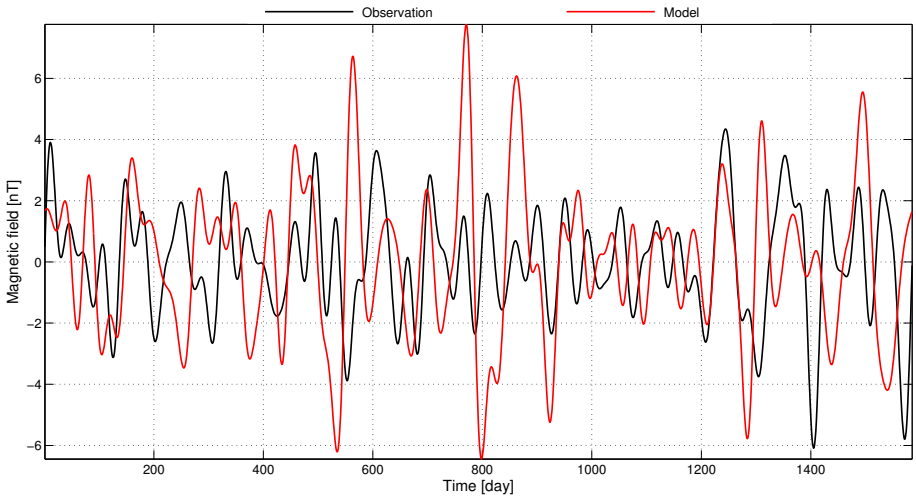

Figure 4.9: For the days 15 May 2011 to 15 September 2015, comparison between the magnetic field measurement (black line) and calculated OGM field (red line) at IPM in the 33- to 135-day period. Time is measured relative to the starting date of the observations.

Table 4.1: Root-mean-square error between observed and calculated OGM signals

Period (days)	RMSE (nT)
33-48	1.17
48-55	1.09
39-48	0.96
39-47	0.83
33-39	0.69
33-38	0.67

are in phase extends to 1050 days, approx., while the amplitude of the observed signal decreases, especially between days 800 to 900. The difference between Figs. 4.13 and 4.14 is produced by the addition of the corresponding 48-day components (green lines in Figs. 4.15 and 4.16) to the observed (black lines in Figs. 4.14 and 4.15) and modelled (red lines in Figs. 4.14 and 4.16) signals.

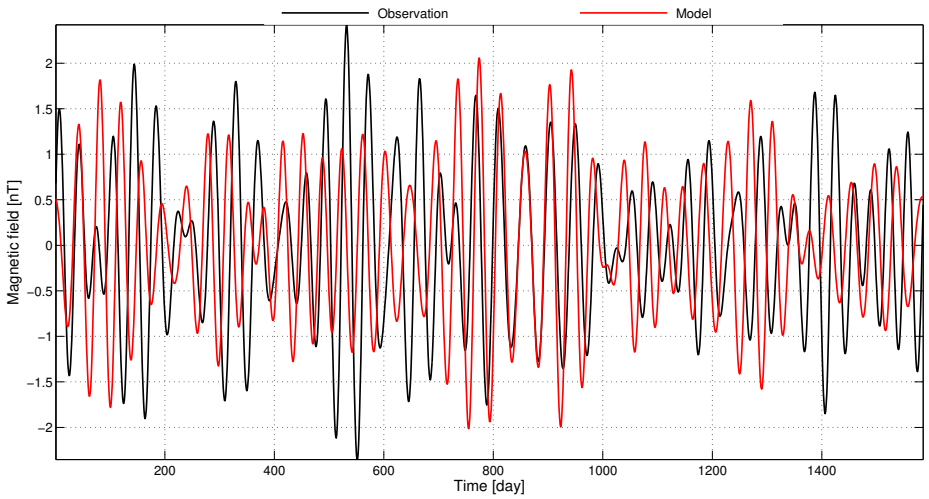

Figure 4.10: For the days 15 May 2011 to 15 September 2015, comparison between the magnetic field measurement (black line) and calculated OGM field (red line) at IPM in the 33- to 48-day period. Time is measured relative to the starting date of the observations.

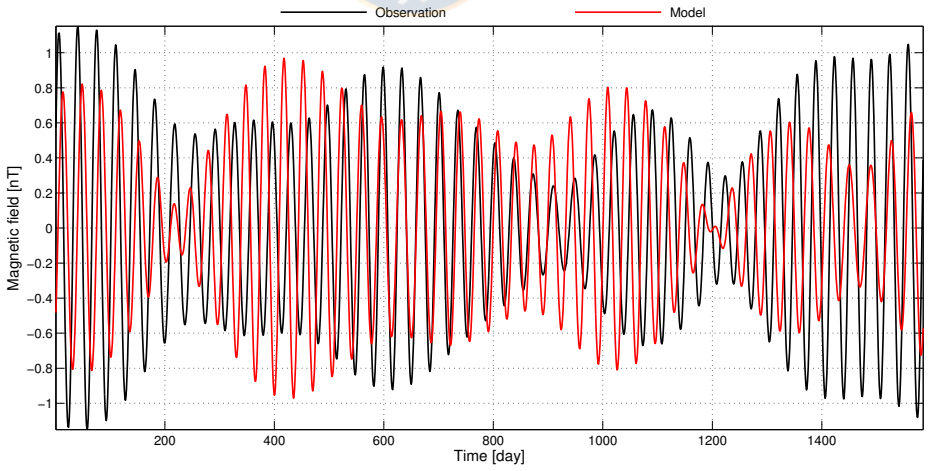

Figure 4.11: For the days 15 May 2011 to 15 September 2015, comparison between the magnetic field measurement (black line) and calculated OGM field (red line) at IPM in the 33- to 38-day period. Time is measured relative to the starting date of the observations.

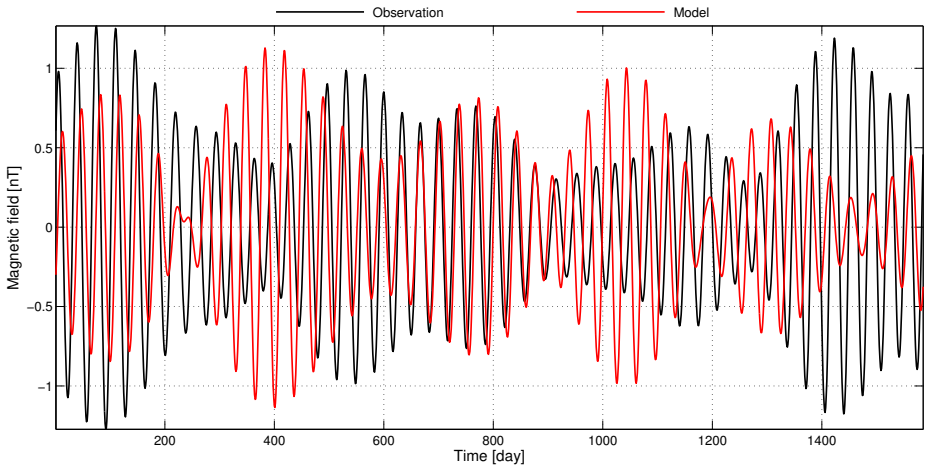

Figure 4.12: For the days 15 May 2011 to 15 September 2015, comparison between the magnetic field measurement (black line) and calculated OGM field (red line) at IPM in the 33- to 39-day period. Time is measured relative to the starting date of the observations.

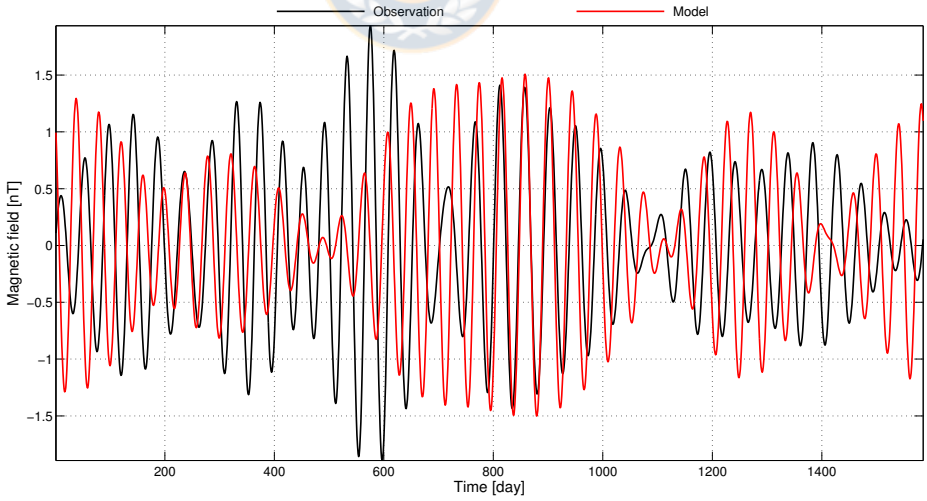

Figure 4.13: For the days 15 May 2011 to 15 September 2015, comparison between the magnetic field measurement (black line) and calculated OGM field (red line) at IPM in the 39- to 48-day period. Time is measured relative to the starting date of the observations.

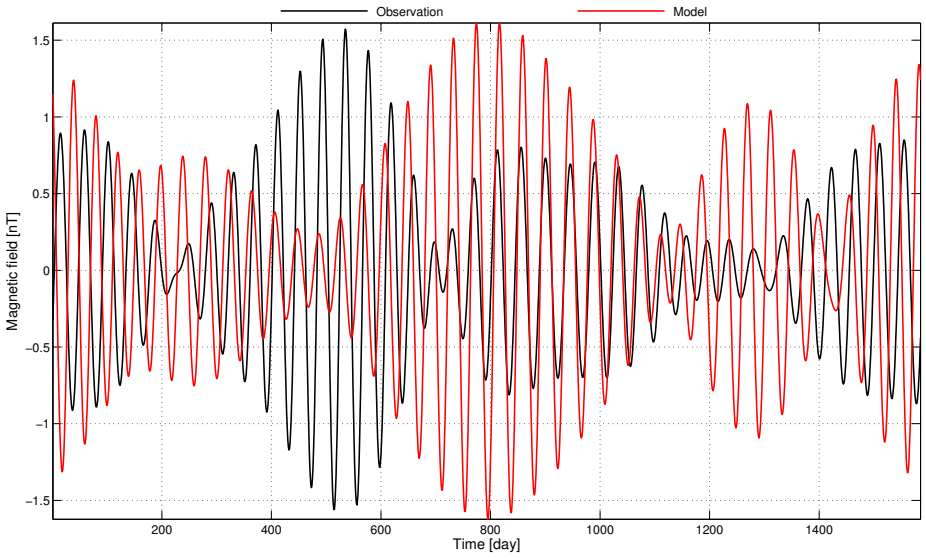

Figure 4.14: For the days 15 May 2011 to 15 September 2015, comparison between the magnetic field measurement (black line) and calculated OGM field (red line) at IPM in the 39- to 47-day period. Time is measured relative to the starting date of the observations.

The dependence of the calculated magnetic field on increasingly larger rectangular areas around IPM at the days 100 (August 22, 2011) and 773 (June 25, 2013), where the Fig. 4.12 shows a trough and a peak, respectively, is depicted in Fig. 4.17. Both panels show that even the contribution of velocity data at great distances from the station is significant, thereby opening possibilities to monitor both meso- and large-scale marine currents. The rise and the magnitude of the OGM field, considering two degrees away from the island, are smaller on the day 100 (Fig. 4.17, left) than on the day 773 (Fig. 4.17, right). This situation is in agreement with the Fig. 4.18, in which the induced electric currents on June 25, 2013, are more intense

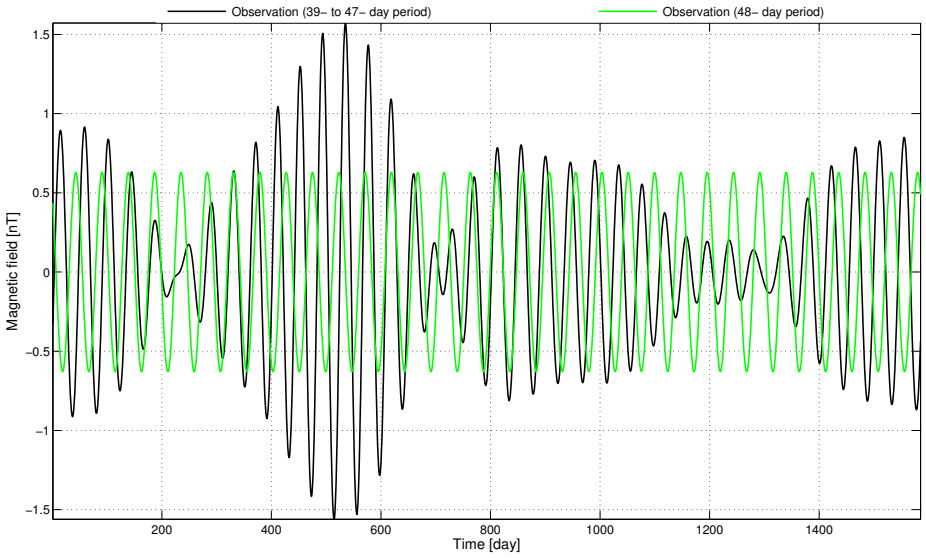

Figure 4.15: For the days 15 May 2011 to 15 September 2015, comparison between the magnetic field measurements at IPM in the 39- to 47-day period (black line) and 48-day period (green line). Time is measured relative to the starting date of the observations.

and curl around the island in a more pronounced form (Fig. 4.18, right), thereby representing a stronger and more divergent velocity field, and suggesting a flux of water to the island.

It is important to recall that the velocity data used in this section are a suitable representation of the currents only in the first 300-500 m, approx. However, in some periods, an intensification of the transport in deeper levels may occur. In that case, data from other sources (e.g., `http://marine.copernicus.eu/`) could be used to calculate the circulation throughout the entire water column instead of using the upper depth interval, leading to changes in the induced magnetic signal. The work of

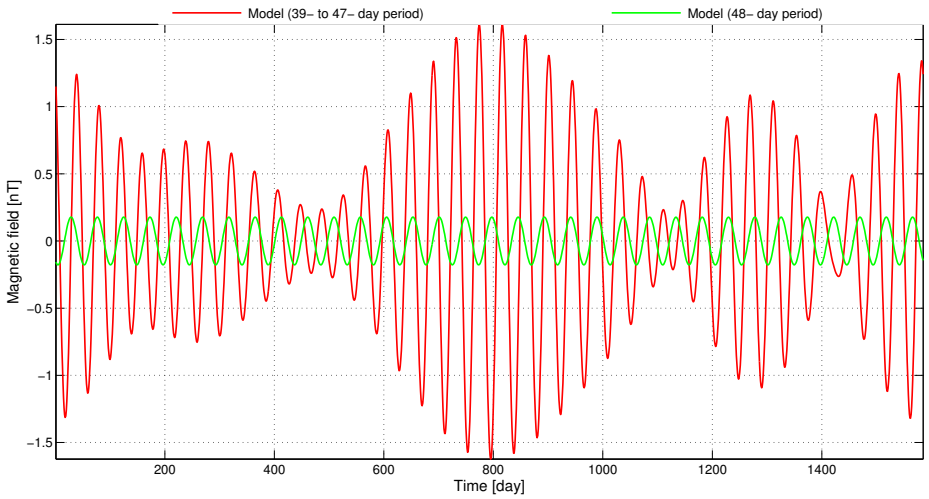

Figure 4.16: For the days 15 May 2011 to 15 September 2015, comparison between the calculated OGM fields at IPM in the 39- to 47-day period (black line) and 48-day period (green line). Time is measured relative to the starting date of the observations.

Irrgang et al. (2018) [23]) is relevant on this topic. They show that ocean-circulation-induced magnetic signals are dominantly generated by electric currents in the upper 2000 m of the ocean basin. In contrast to the model used in this thesis (Eqs. 3.1- 3.2), which reduces the ocean to a single, homogeneous thin layer, their three-dimensional model can resolve vertical variations of electric currents. For example, following their procedure, the contribution to OGM signals of the wind-driven convergence (divergence) of the transport in the surface Ekman layer, provided by the downwelling (upwelling), could be verified.

4.3. Discussion

The motion of electrically-conducting seawater through the Earth's magnetic field induces electric currents in the ocean, which in turn generate secondary OGM fields,

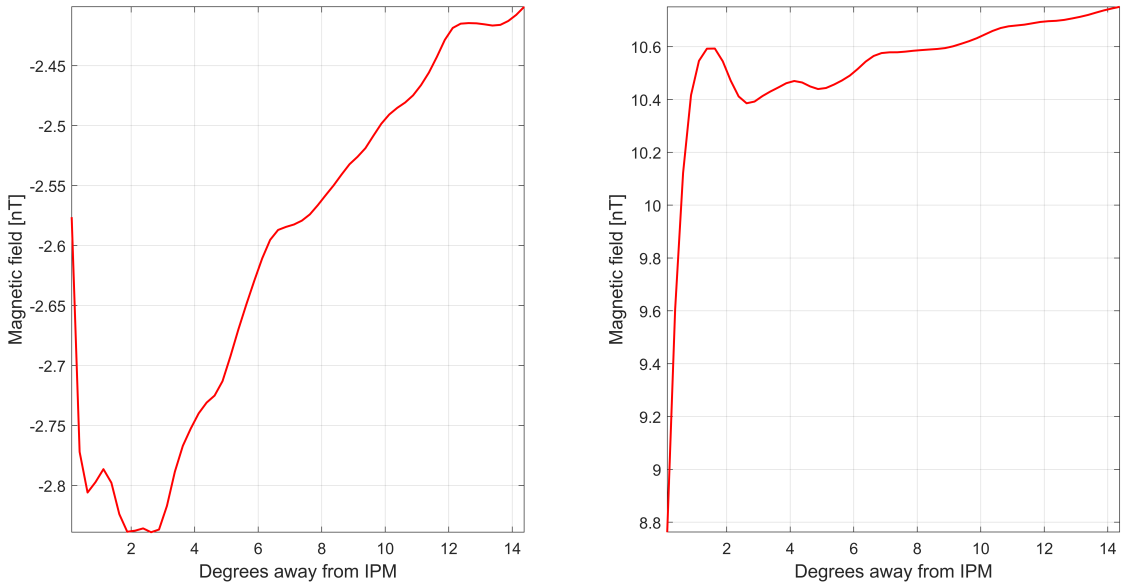

Figure 4.17: For the days August 22, 2011 (left) and June 25, 2013 (right), dependence of the calculated OGM field at IPM on distance from the station.

detectable outside the ocean layer by land-based magnetometer stations. This thesis was focused on studying the influence of two kind of oceanic processes in the vertical component of the Earth's magnetic field, recorded at a magnetic observatory in Easter Island: tsunamis and mesoscale processes. The magnetic records were compared with the results of a numerical model based on the Biot-Savart law. The oceanic electric currents were calculated using velocity data, from tsunami simulations and satellite altimetry, in a rectangular region around the Easter Island. The model reproduces the main features of the magnetic disturbances recorded during the 2010 and 2015 tsunami events. In the case of observations in the period from May 2011 to September 2015, the model is in a good agreement with data in a specific period band. Both findings suggest that the observed data may be caused by oceanic electric currents.

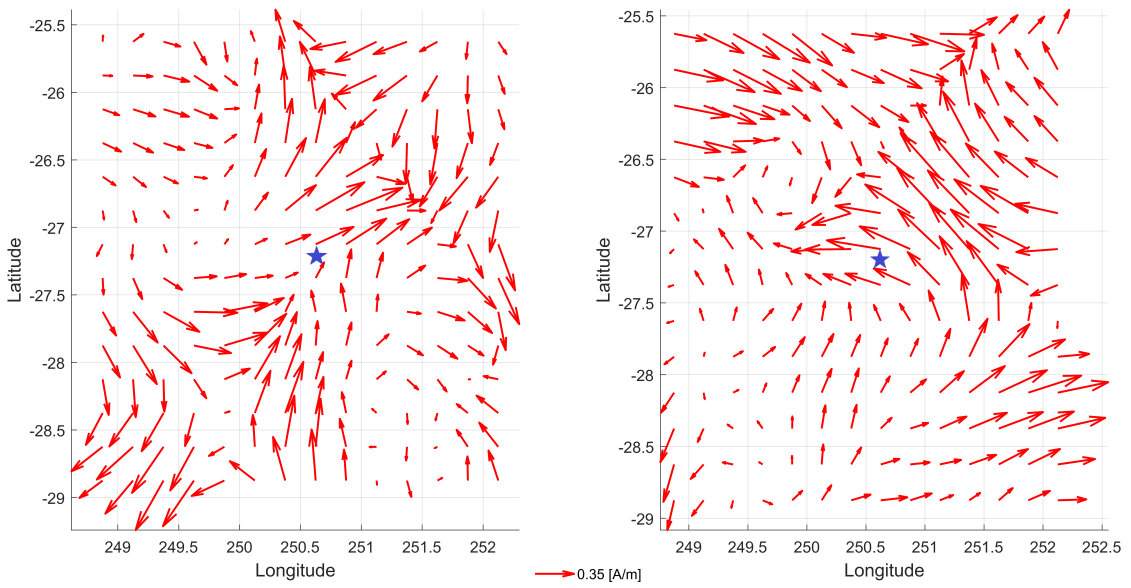

Figure 4.18: Induced electric currents (red arrows) in a rectangular area of up to two degrees around IPM (blue star) on August 22, 2011 (left) and June 25, 2013 (right).

Observed and calculated magnetic signals at IPM between 11:00 and 14:00 UTC during the 2010 event were presented by Wang et al. (2015) [74] (see their Fig. 4). This time interval corresponds to 265-445 min in Fig. 4.2. When compared with the measured data from 325 to 360 min, the computed waveform in Fig. 4.2 represents an improvement to their simulation. To estimate the magnetic field, Wang et al. (2015) [74] used a formula (derived by Tyler 2005 [65] and based in Eq. 4.3 in next page) which directly relates the expected magnetic perturbation to the sea surface displacement at a location of interest:

$$\frac{b_z}{F_z} = \frac{c_0}{c_s}\frac{\xi}{H}e^{-\kappa z}, \tag{4.2}$$

where $c_s = c_0 + i \cdot (2/\mu_0\sigma_s H)$, $c_0 = \sqrt{gH}$ is the phase speed of the tsunami wave under the shallow-water theory, and the term $e^{-\kappa z}$ represents the exponential decay

of the magnetic field strength depending on the height above the sea surface, z, and a wavenumber component, κ, of the tsunami.

Wang et al. (2015) [74] focused the analysis in the leading wave and considered sea surface elevations from four virtual mareographs located two degrees around Easter Island, since Eq. 4.2 is valid only where the water column does not have important variations in the horizontal compared to the velocity field, i,e., in the deep ocean, far from continental shelves and coastlines. This restriction appears from neglecting the terms $\partial_x D$ and $\partial_y D$ in the LHS of Eq. 2.11. On the other hand, the model developed in this thesis considers data from each grid cell, even where the bathymetry may changes abruptly, thereby probably explaining the better fit to the measurement, at least for a good part of the tsunami trailing waves in Fig. 4.2.

Although no amplitude attenuation of b_z due to the Faraday-induced electric field (opposite to $\vec{u} \times \vec{F}$) is expected to be described in this thesis, some comments about this topic are necessary. Taking the curl of Eq. 2.3, combining with Eq. 2.2, and assuming an homogeneous conductivity, the magnetic induction equation is obtained:

$$\partial_t \vec{B} = \nabla \times (\vec{u} \times \vec{B}) - \nabla \times (K \nabla \times \vec{B}), \tag{4.3}$$

where $K = (\mu_0 \sigma_s)^{-1}$. The source term, $\nabla \times (\vec{u} \times \vec{B})$, due to a prescribed ocean velocity field is balanced by the self-induction term, $\partial_t \vec{B}$, and the magnetic dissipation term, $\nabla \times (K \nabla \times \vec{B})$. Using 2-D-time-domain numerical calculations, the dependence of Eq. 4.3 on the ocean depth for a tsunami flow coupled with the geomagnetic field was investigated by Minami et al. (2015) [46] based on the dimensionless magnetic

Reynolds number:

$$Rm = \frac{UL}{K}, \tag{4.4}$$

which compares the relative magnitude of the two terms in the RHS of Eq. 4.3 (Bittencourt 2004 [7]). In Eq. 4.4, U and L are typical velocity and length scales, respectively, of the motion. Using $U = \sqrt{gH}$ and $L = H$, Minami et al. (2015) [46] found that as the water depth increases, the influence of the diffusion term attenuates, while the self-induction term must become larger to balance the flow term.

Replacing $U = L/T$, with T as time scale, and using the wavelength instead of ocean depth as the length scale of the motion in Eq. 4.4, the self-induction effect tends to become unimportant for subinertial flows (such as those related to Figs. 4.10- 4.18). For example, using $L = 200$ km and $T = 20$ days, Eq. 4.4 gives an induction number of 0.1. On the other hand, for a tsunami flow with typical values $L = 100$ km and $T = 20$ min, $Rm = 42 \gg 1$, which corresponds to a self-induction dominant case. Using the wavelength instead of ocean depth as length scale is in accordance with previous works (Podney 1975 [49]; Chave and Luther 1990 [12]), and the self-induction effect should be considered in the tsunami case.

Figs. 4.19-4.20 show comparisons between the magnetic measurements at IPM and numerical calculations using the models developed in this thesis and by Tatehata et al. (2015) [61]. Their mechanism considers the self-induction term by solving Eq. 4.3 for b_z using appropiate boundary conditions. Tatehata et al. (2015) [61] calculated the electric currents at each grid point based in the analytical solution of Tyler (2005) [65], and then integrated the induced magnetic fields using the Biot-Savart

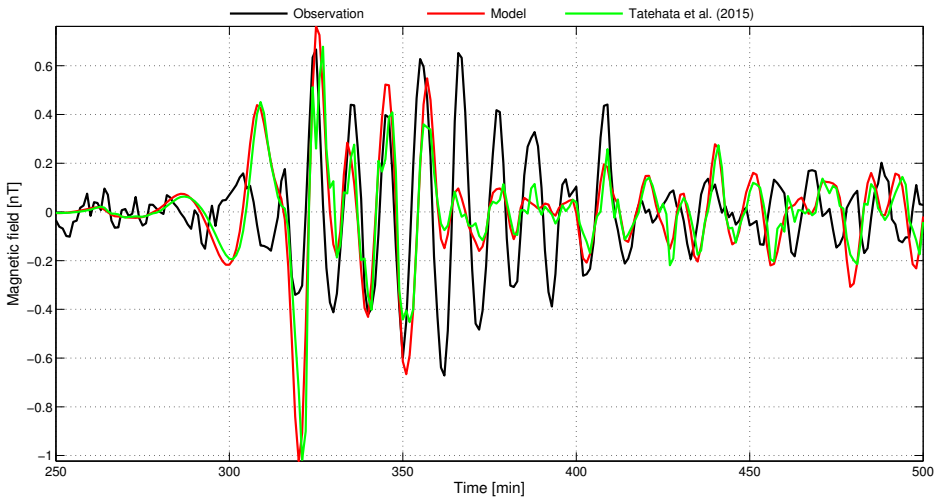

Figure 4.19: Comparison between the magnetic field measurement (black line), calculated TGM field (red line), and calculated TGM field using the model of Tatehata et al. (2015) [61] (green line) at IPM, for the 2010 Chile tsunami, considering a resolution of 1.08 arcmin for the second level grid around Easter Island. Time is measured relative to the earthquake origin time. (From Torres et al. 2019 [64].)

law. The application of his method in this work required a great computational cost while using refined bathymetries. Therefore, a coarser resolution –1.08 arcmin– for the second level grid around Easter Island was considered. No significant improvements of the fit between observations and models are noted, which might be explained since the self-induction effect starts to decrease as the ocean becomes shallow (specifically, with depths $H < 5$ km), according to the Fig. 4 of Minami et al. (2015) [46]. Therefore, the choice of the magnetostatic method described in this thesis seems reasonable.

A realistic consideration of the seawater conductivity, instead of an homogeneous value, could have influence on the results. For example, since the temperature in

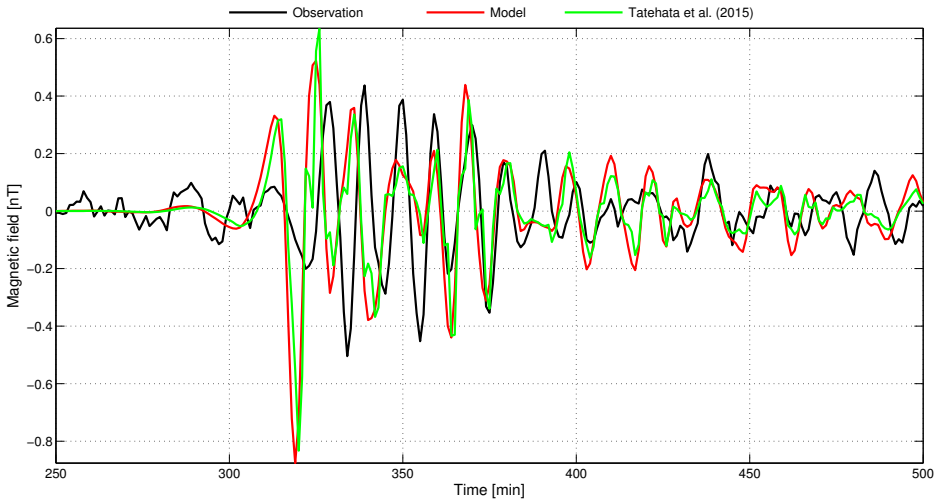

Figure 4.20: Comparison between the magnetic field measurement (black line), calculated TGM field (red line), and calculated TGM field using the model of Tatehata et al. (2015) [61] (green line) at IPM, for the 2015 Chile tsunami, considering a resolution of 1.08 arcmin for the second level grid around Easter Island. Time is measured relative to the earthquake origin time. (From Torres et al. 2019 [64].)

the ocean decreases with depth, a decreasing 1-D conductivity profile might be a suitable approximation. In any case, considering a conductivity profile would involve a vertically averaged and conductivity weighted velocity (Sanford 1971 [54]) in order to calculate the Eq. 3.2:

$$\vec{u}_h^* = \frac{\int_{-H+\eta}^{\xi} \sigma_s \vec{u}_h dz}{\int_{-H+\eta}^{\xi} \sigma_s dz}. \tag{4.5}$$

Conductivity-weighted ocean velocities are important in the case of investigating oceanic heat and salinity altering processes. Covering a period of 50 years, Petereit et al. (2018) [48] compared computed sea surface temperature and OGM anomalies,

finding that the latter contain information for an early awareness of developing anomalous warm and cold El Niño–Southern Oscillation conditions in the Pacific Ocean, which are associated with very large fluctuations in the temperature, and therefore change the electric conductance distribution in the ocean. Obviously, this kind of processes are more related to the results showed in Figs. 4.7- 4.18 than those derived for the tsunami events.

In addition to the influence of a depth-dependent seawater conductivity, horizontal derivatives of this parameter, e.g., an island-ocean conductivity contrast, could also play a role in the results. Using Eq. 4.3 and splitting the resistivity $1/\sigma_s$ into radially and laterally varying parts, a non-trivial secondary PM field, generated from the TM component, couples to the primary PM measurements on land, close to the oceanic shorelines (Velímský et al. 2019 [72]). Although such an effect was found to be negligible for measurements of b_z at an island site during the 2011 Tohoku-Oki tsunami (Zhang et al. 2014 [79]), this transfer of energy from TM to the observable ocean-induced PM modes above the ocean surface, due to lateral heterogeneities of electrical conductivity, might be investigated in future studies of Easter Island.

As suggested in the Introduction part, due to its strategic location, data from IPM represent a promising source of information for studying the activity in the south Pacific subtropical gyre. For example, based on Eq. 4.5, and using the same grid region around the island and the magnetic data, changes in salinity and temperature distributions could be monitored using OMCT, which calculates temporal variable distributions of salinity, temperature and velocities as sources for the induction of OGM fields (see Saynisch et al. 2016 [57]; Irrgang et al. 2018 [23]). A

future refinement of the model from this thesis using OMCT could conduce to an improvement of the results.

Comparisons of induced magnetic fields from different data sources, e.g., planetary indices of geomagnetic activity, could serve as a complement to the use of numerical models, and provide hints of time intervals where the influence of oceanic processes in the geomagnetic field are most probable. An example are the Ap values (Fig. 4.21), which can be considered as a measurement of solar corpuscular emmisions, from the coronal holes, by its magnetic effects in the Earth (Ahluwalia 1998 [1]). In general, time series of Fig. 4.21 have similar trends and orders of magnitude, despite some extreme Ap values and time intervals where differences between the curves are more noticeable. Some differences might be explained, for example, by an influence of subsurface ocean currents below 500 m, as mentioned on page 42.

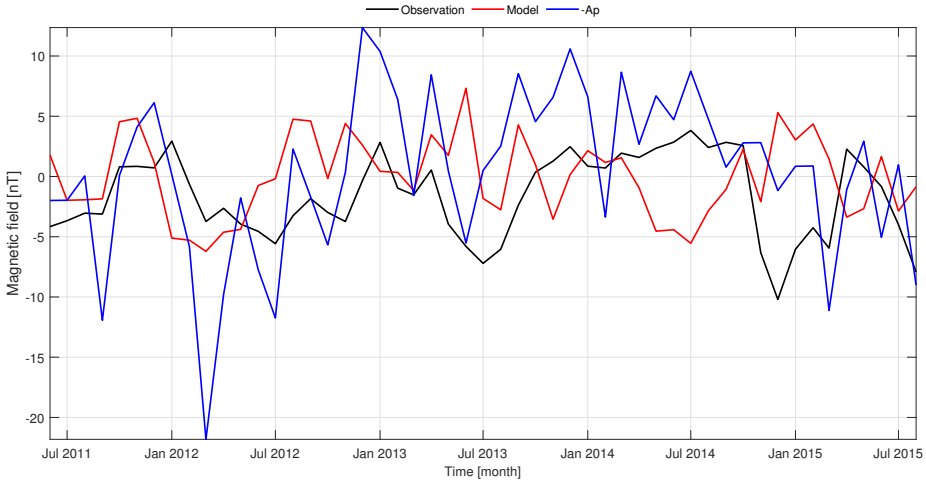

Figure 4.21: Comparison between monthly means of magnetic field measurements (black line) and calculated OGM fields (red line) at IPM, and Ap-derived magnetic fields (blue line), during the 2011-2015 period. Ap-derived magnetic fields were calculated using the original monthly mean values of the Ap index, which are expressed in units of 2 nT (Menvielle and Berthelier 1991 [41]). The latter are available at `https://www.gfz-potsdam.de/en/kp-index/`.

Chapter 5

CONCLUSIONS

In this thesis, the presence of OGM signals at the Easter Island Observatory during two earthquake-induced tsunamis (in 2010 and 2015) and during the 2011-2015 period was investigated. Using a magnetostatic model, observed perturbations in the vertical component of the geomagnetic field resulted in good agreement with the model in specific period bands. General conclusions, along with some possible guidelines, can be summarized as follows:

- The results of Figs. 4.3-4.4 suggest that even a relatively small tsunami (for example, compared with 2010 Mw8.8 Chile and 2011 Mw9.0 Japan tsunamis), such as the one produced by the 2015 Mw8.2 earthquake, induces an observable magnetic perturbation due to the water movement. This is the first study that uses a numerical approach to explain the magnetic variation due to the 2015 event. In the case of the 2010 event, the results (Figs. 4.1-4.2) support the hypothesis, proposed by Manoj et al. (2011) [38] and Wang et al. (2015) [74], of an oceanic origin of the signals. This is also the first study where the influence of mesoscale marine currents (Figs. 4.10-4.18) in the magnetic field at Easter Island is investigated.

- As the results of the model can reproduce the main features, but not all, of

the observed magnetic fields, the influence of non-oceanic electric currents in the magnetic data, specially in time intervals where the model does not fit the observations, should not be ruled out. In order to decide whether a ground-level magnetic field perturbation is due to electric currents in the ocean or, for example, the ionosphere, numerical calculations considering both zones are necessary. A suitable model might be the Thermosphere Ionosphere Mesosphere Electrodynamics General Circulation Model (TIME-GCM), used by Schnepf et al. (2018) [59] to predict semidiurnal lunar tidal magnetic signals, which were compared to data from global geomagnetic observatories. Although according to their work, not much influence of the ionosphere is expected in our study area (at least for semidiurnal periods), a comparison of IPM's data with TIME-GCM's predictions might be verified, thereby representing a future complement to this thesis.

- The magnetic anomalies recorded at the IPM station might be caused by a combination of electric currents in the ocean, the ionosphere, or their induced counterparts due to mutual inductance. Therefore, the observed magnetic anomalies could be due to a combination of primary and induced electric currents (Tyler et al. 2017 [69]; Sorokin et al. 2019 [60]). The contribution of these effects could even validate the first oscillations in the calculated signals (Figs. 4.2 and 4.4). Furthermore, magnetic disturbances generated via TAI coupling can appear both after and before a tsunami arrival throught the so-called co- and ahead-of- tsunami traveling ionospheric disturbances (Kherani et al. 2016 [26]), which were proposed by Klausner et al. (2016) [27], using a wavelet analysis, as an explanation for the disturbances in data from ground-based magnetometer observatories (IPM, among them) during the 2015 event.

- Differently from Wang et al. (2015) [74], whose work was focused on reproducing the perturbation produced by the leading wave, the model developed in this thesis can predict at least a good part of the trailing waves of the tsunami (Fig. 4.2). For purposes of warning, not only the tsunami wave front but also the trailing waves are important. When a train of waves approaches a coastal region, the varying topography refracts and traps part of the tsunami energy, triggering unexpected progressive and standing waves on continental shelves and coastal areas even hours after an earthquake, leading to episodes of confusion among the population (Bellotti et al. 2012 [5]). For example, the constructive interference of these kind of waves produced devastating effects three hours after the onset of the 2010 earthquake at Talcahuano, Chile, which was located 100 km south of the epicenter (Yamazaki and Cheung 2011 [78]). Moreover, tsunami-island interaction causes that wavefronts travel around an island, extending the tsunami menace even to the coastline segments potentially protected from the main tsunami attack (Tinti and Vannini 1994 [62]; Bai et al. (2015) [4]). Tsunami-triggered waves could also produce ionospheric disturbances, as suggested by Kherani et al. (2016) [26] for the 2011 Tohoku-Oki tsunami, and detectable perturbations in the geomagnetic field (see Appendix A). A detailed study of these long-lasting phenomena and its influence in data from INTERMAGNET observatories across the Pacific Ocean might be considered in a future research. As a support, the work of Bai et al. (2015) [4] revealed persistent oscillation patterns, following the 2011 Tohoku-Oki tsunami, across the entire Pacific basin over a wide period range (5-700 min).

- The original motivation (and hypothesis) of this thesis was to investigate whether both dispersive tsunami waves and tsunami-triggered waves, such as edge

waves, could produce a detectable effect in the local magnetic field. At least using COMCOT for both 2010 and 2015 Chilean tsunamis, dispersion was found to be almost irrelevant, despite some isolated, short time intervals. However, edge waves could induce detectable perturbations, as calculated in the Appendix A.

- Especially important for some of our research groups, e.g., CHIOOS (Chilean Integrated Ocean Observing System) or CInFAA (Centro Interuniversitario de Física de la Alta Atmósfera), is monitoring both ocean and ionospheric activities along the Chilean coast. Encouraged by the results obtained in this thesis and in previous studies, a land-based magnetometer was installed in Bahía de San Vicente, close to Concepción, and its produced data will be presented in future works. For example, modelled magnetic perturbations, forced with regional ocean models, could be compared with both TIME-GCM's predictions and magnetometer data from different sources (our magnetometer, SAMBA, INTERMAGNET, etc.)

- This study shows that the influence of marine currents in the Earth's magnetic field is significant, that this physical process can be adequately described with accessible numerical tools, and that it can be an instrument for monitoring the ocean, whether on minute (tsunamis) or monthly and larger (ocean circulation) timescales.

Appendix A

EDGE WAVES IN THE OCEAN

The LSW version of Eqs. 2.9-2.11, without account of volumetric fluxes, bottom friction and Coriolis force, is:

$$\partial_t \vec{u} = -g\nabla\xi, \tag{A.1}$$

$$\partial_t \xi + \nabla \cdot (H\vec{u}) = 0. \tag{A.2}$$

The use of Eqs. A.1-A.2 is quite reasonable since the wavelengths of trapped waves are long compared to the depth of the water (Mei et al. 2005 [40]). Eliminating $\vec{u}$:

$$g\nabla \cdot (H\nabla\xi) = \partial_t \partial_t \xi. \tag{A.3}$$

If the waves are sinusoidal in time, time and space dependences may be separated:

$$\xi(x, y, t) = \phi(x, y)e^{-i\omega t}, \tag{A.4}$$

$$\vec{u}(x, y, t) = \vec{u}(x, y)e^{-i\omega t}. \tag{A.5}$$

From Eqs. A.1-A.2, the spatial factors are related by:

$$\vec{u} = -\frac{ig}{\omega}\nabla\phi. \tag{A.6}$$

$$i\omega\phi = \nabla \cdot (H\vec{u}). \tag{A.7}$$

Combining Eqs. A.6-A.7:

$$\nabla \cdot (H\nabla\phi) + \frac{\omega^2}{g}\phi = 0. \tag{A.8}$$

As a special case of depth variation, consider a straight and long beach with constant slope. Let the mean shoreline coincide with the y- axis, and let the water be in the region $x > 0$ (Mei et al. 2005 [40]). The bottom is described by:

$$z = -H = -sx, \quad x > 0, \quad s = const. \tag{A.9}$$

A solution suitable in this case (ξ harmonic in time as well as in alongshore direction) is:

$$\xi(x, y, t) = \phi(x)e^{i(k_y y - \omega t)}. \tag{A.10}$$

Eq. A.8 gives:

$$x\xi'' + \xi' + \left(\frac{\omega^2}{sg} - k_y^2 x\right)\phi = 0. \tag{A.11}$$

By the following transformation:

$$\zeta = 2k_y x, \quad \phi = e^{-\frac{\zeta}{2}} f(\zeta), \tag{A.12}$$

Eq. A.11 can be rewritten as:

$$\zeta f'' + (1-\zeta) f' + \left(\frac{\omega^2}{2k_y sg} - \frac{1}{2} \right) f = 0. \tag{A.13}$$

Nontrivial solutions exist when ω corresponds to the discrete values:

$$\frac{\omega_n^2}{2k_{yn} sg} = n + \frac{1}{2}, \quad n = 0, 1, 2, 3, ... \tag{A.14}$$

Eq. A.14 is the shallow-water dispersion relation for mode-n edge waves, considering very gentle bottom slopes (given that $s \approx \tan s$). It can be expressed as:

$$c_n = \omega_n / k_{yn} = \frac{gT_n}{2\pi}(2n+1)s, \quad n = 0, 1, 2, 3, ... \tag{A.15}$$

where c_n and T_n are phase velocity and period of the nth mode. Using Eq. A.14 in Eq. A.13:

$$\zeta f'' + (1-\zeta) f' + nf = 0, \quad n = 0, 1, 2, 3, ... \tag{A.16}$$

which is the Laguerre's equation. Solutions are the Laguerre polynomials:

$$f_n(\zeta) = \frac{e^\zeta}{n!} \frac{d^n}{d\zeta^n}(e^{-\zeta}\zeta^n). \tag{A.17}$$

For example, using Eq. A.12, the first three modes associated with Eq. A.17 are:

$$\phi_0 = e^{-k_y x}, \quad \phi_1 = (1 - 2k_y x)e^{-k_y x}, \quad \phi_2 = (2(k_y x)^2 - 4(k_y x) + 1)e^{-k_y x}. \tag{A.18}$$

Eq. A.10 becomes:

$$\xi_n(x, y, t) = e^{-k_y x} f_n(\zeta) e^{i(k_y y - \omega t)}. \tag{A.19}$$

The energy of these modes is trapped against the coast. The velocity components of the nth mode $\vec{u}_n = (u_n, v_n)$ are obtained using Eqs. A.5,A.6,A.10,A.12, and A.17:

$$\vec{u}_n(x, y, t) = \frac{g}{\omega} e^{-k_y x} e^{-i(\omega t - k_y y + \pi/2)} (\partial_x f_n(\zeta(x)) - k_y f_n(\zeta(x)))\hat{x} + i k_y f_n(\zeta(x))\hat{y}, \tag{A.20}$$

where $\hat{x}$, $\hat{y}$ are the unitary vectors in the x- and y- directions, respectively. For example, the velocity field for the mode-0 progressive edge wave can be expressed as:

$$\vec{u}_0(x, y, t) = -\frac{gT}{\lambda_y} e^{-2\pi/\lambda_y} \left(\cos(\omega t - k_y y + \pi/2)\hat{x} + \sin(\omega t - k_y y + \pi/2)\hat{y}\right). \tag{A.21}$$

Combining Eq. A.21 with the source electric current, $\sigma_s(\vec{u_0} \times \vec{F})$, and the Ampere's law, and solving for b_z:

$$b_z = \mu_0 \sigma_s H F \frac{gT}{\lambda_y}. \tag{A.22}$$

Assigning the following realistic orders of magnitude for physical variables: $\mu_0 = 4\pi \times 10^{-7}$ N/A^2, $\sigma_s = 4$ S/m, $H = 100$ m, $F = 20000$ nT, g =9.8 m/s^2, $T = 24$

min, $\lambda_y = 80$ km (latest two values as an example, based in the study of Munger and Cheung 2008 [47]), gives a value of about b_z =1.8 nT, which is detectable by a magnetometer.

Appendix B

INTRODUCCIÓN

Los iones de sodio y cloro disueltos en el océano constituyen la gran mayoría de los portadores de carga que contribuyen a su conductividad eléctrica. Cuando el agua de mar -eléctricamente conductora- se mueve a través del campo magnético terrestre, los iones de sal son desviados de su trayectoria por su interacción con este campo y su movimiento produce un flujo contínuo de corrientes eléctricas en el océano. Estas corrientes producen débiles, aunque detectables, campos magnéticos secundarios alrededor de ellas, en el orden de los nanotesla (nT). Estas perturbaciones magnéticas pueden ser detectadas desde estaciones geomagnéticas instaladas en tierra, en el fondo del mar, e incluso desde altitudes satelitales (Larsen 1968 [32]; Minami 2017 [42]). Varios procesos oceánicos, como las ondas internas (Pukhtyar y Kukushkin 1996 [52]), remolinos de mesoescala (Lilley et al. 1993 [36]), tsunamis (Tatehata et al. 2015 [61]), mareas semi-diurnas y diurnas (Larsen 1968 [32]; Tyler et al. 2003 [67]; Saynisch et al. 2017 [56]; Schnepf et al. 2018 [59]) y la circulación de gran escala (Manoj et al. 2006 [37]; Saynisch et al. 2018 [55]), entre otros, producen señales magnéticas detectables. Hoy en día, incluso eventos asociados a El Niño – Oscilación del Sur se pueden encontrar en señales magnéticas (Petereit et al. 2018 [48]).

La importancia de monitorear el campo geomagnético se puede ilustrar con algunos ejemplos:

- Las tormentas geomagnéticas pueden interrumpir nuestros sistemas globales de comunicaciones y de distribución de energía eléctrica (Gonzalez et al. 1994 [17]).

- Según algunos autores (Minami et al. 2015 [46]; Schnepf et al. 2016 [58]; Minami et al. 2019 [43]), mediante el mecanismo descrito en el primer párrafo, durante un tsunami se generan anomalías magnéticas detectables incluso antes de la llegada de las olas.

- Temperatura y salinidad son las variables que más influyen en la conductividad eléctrica del océano, y las mediciones de campo magnético terrestre contienen información sobre el transporte global de agua, calor y salinidad en el océano (Tyler et al. 1999 [68]; Irrgang et al. 2019 [22]).

De los ejemplos mencionados, los tsunamis son especialmente relevantes para nuestro país. Con respecto a su generación, el Océano Pacífico es considerado como la región más peligrosa del mundo, y frecuentemente están ocurriendo terremotos alrededor del perímetro llamado Anillo de Fuego (Levin y Nosov 2016 [34]). Las señales magnéticas generadas por los tsunamis pueden ser producidas por corrientes eléctricas no solo en el océano sino también en la ionosfera, región de la atmosfera que está entre 60 y 1000 km, aprox., sobre la Tierra (Campbell 2003 [9]), y que contiene la más alta concentración de electrones libres. Estas corrientes eléctricas en la ionosfera son causadas por perturbaciones atmosféricas, generadas a su vez por oscilaciones sísmicas de la tierra o el tren de ondas del tsunami, las cuales se propagan hacia la ionosfera. Estos mecanismos se denominan acoplamientos tsunami-atmosfera-litosfera

(LAI) (Klausner et al. 2017 [28]) y tsunami-atmosfera-ionosfera (TAI) (Kherani et al. 2012 [25]), respectivamente. Reconocer el principio físico que genera una perturbación magnética es un gran desafío, ya que a cada instante de tiempo una combinación de señales de órdenes de magnitud comparables y provenientes de distintas partes de la Tierra (océano, ionosfera, magnetósfera, etc.) contribuyen a una observación en un lugar en específico (Campbell 2003 [9]). Este desafío puede comprobarse en algunas discrepancias entre estudios relacionados con señales magnéticas generadas por tsunamis.

Durante el tsunami de Chile del año 2010 (Mw8.8), un observatorio magnético (27.17 S, 109.41 W) en la Isla de Pascua (código IPM, de acuerdo a la red de observatorios magnéticos INTERMAGNET), ubicado a unos 3500 km al oeste de la costa chilena, capturó una señal periódica de 1 nT en la componente vertical del campo geomagnético (Manoj et al. 2011 [38]), coincidentemente con el paso del tsunami por la isla. Comparando las mediciones con un modelo numérico, Wang et al. (2015) [74] propusieron un posible origen oceánico de las corrientes eléctricas que generaron dicha perturbación. Por su parte, Klausner et al. (2014) [29] analizaron las mediciones de IPM utilizando la transformada wavelet, y asociaron los periodos dominantes en el espectro de potencia al acoplamiento TAI. Durante el tsunami de Chile del año 2015 (Mw8.2), IPM nuevamente mostró una perturbación de alrededor de 1 nT en la componente vertical, coincidentemente con la hora de llegada del tsunami. Siguiendo un procedimiento similar al de Klausner et al. (2014) [29], Klausner et al. (2016) [27] sugirieron que, a través del mecanismo TAI, las corrientes eléctricas generadoras del campo magnético secundario tendrían un origen ionosférico. A diferencia del tsunami de 2010, para este evento no existen estudios que usen modelos numéricos para

comprobar el origen de las corrientes.

Además de la detección de tsunamis, los datos de IPM también podrían ser usados para investigar la presencia de remolinos de mesoescala. Estos remolinos dominan la variabilidad de las corrientes oceánicas en los primeros cientos de metros y en periodos de 30-90 días, y pueden transportar calor, nutrientes y organismos hacia y alrededor de la Isla de Pascua. La isla se encuentra en el límite oriental del giro subtropical anticiclónico del Pacífico sur, el cual se caracteriza por un nivel muy bajo de nutrientes y un alto grado de endemismo (von Dassow y Collado-Fabbri 2014 [73]). La conexión entre la variabilidad de propiedades físicas y biológicas en el giro se produce en varias escalas espaciales y temporales, las cuales no han sido completamente entendidas hasta ahora. Las señales medidas en IPM podrían representar un punto de partida en esta área de investigación. Un ejemplo de esta conexión físico-biológica es que la mezcla vertical, el bombeo de Ekman y el desplazamiento de la termoclina son los principales mecanismos impulsores de los cambios estacionales observados en la concentración de clorofila en el giro (McClain et al. 2004 [39]).

Considerando lo expuesto, el objetivo de esta tesis es investigar la posible influencia de procesos oceánicos en los datos geomagnéticos registrados en el Observatorio de la Isla de Pascua, en dos casos particularmente relevantes para Chile: tsunamis y circulación oceánica. La metodología utilizada consiste en comparar los datos del observatorio con los resultados de un modelo numérico en tres períodos de tiempo: durante los tsunamis de 2010 y 2015, provocados por terremotos en Chile, y durante el período 2011-2015. El modelo numérico es calculado a partir de la ley de Biot-Savart y velocidades oceánicas en un área rectangular alrededor de la Isla de Pascua.

Las velocidades son obtenidas de simulaciones numéricas de tsunamis y datos de altimetría satelital.

La tesis está dividida en las siguientes secciones: Theoretical Considerations (Marco Teórico), Methodology (Metodología), Results and Discussion (Resultados y Discusión), y Conclusions (Conclusiones).

Appendix C

DISCUSIÓN

El movimiento del agua de mar a través del campo magnético de la Tierra induce corrientes eléctricas en el océano, las cuales a su vez generan campos magnéticos secundarios. Estas perturbaciones pueden ser detectadas fuera del océano, en observatorios magnéticos instalados en tierra. Esta tesis se centró en el estudio de la influencia de dos tipos de procesos oceánicos en la componente vertical del campo magnético de la Tierra, registrada en un observatorio magnético en la Isla de Pascua: tsunamis y procesos de mesoescala. Los datos del observatorio fueron comparados con los resultados de un modelo numérico basado en la ley de Biot-Savart. Las corrientes eléctricas en el océano se calcularon utilizando datos de velocidad, provenientes de simulaciones de tsunamis y altimetría satelital, en una región rectangular alrededor de la Isla de Pascua. El modelo reproduce las principales características de los datos registrados durante los tsunamis de 2010 y 2015. En el caso de las observaciones registradas durante el período de mayo de 2011 a septiembre de 2015, el modelo coincide con éstas en un rango de períodos específico. Ambos hallazgos sugieren que, efectivamente, los datos pueden haber sido causados por corrientes eléctricas inducidas en el océano.

En el año 2015, Wang et al. (2015) [74] realizaron una comparación entre me-

diciones y señales modeladas en la estación IPM durante el tsunami de 2010 (ver intervalo entre 11:00 y 14:00 UTC en su Fig. 4). El intervalo de tiempo mostrado corresponde a los 265-445 min en la Fig. 4.2. Al comparar los resultados mostrados en esta última figura con los datos medidos entre 325 y 360 min, se observa una mejoría con respecto a la Fig. 4 de Wang et al. (2015) [74]. Para calcular el campo magnético, Wang et al. (2015) [74] utilizaron la Ec. 4.2 (propuesta por Tyler 2005 [65] y basada en la Ec. 4.3), la cual relaciona directamente la perturbación con el nivel del mar en el lugar de interés. En dicha ecuación, $c_s = c_0 + i \cdot (2/\mu_0 \sigma_s H)$, $c_0 = \sqrt{gH}$ es la velocidad de fase de la onda de tsunami bajo la aproximación de aguas someras, y el término $e^{-\kappa z}$ representa el decaimiento exponencial, dependiente de la posición sobre el nivel del mar, z, y la frecuencia espacial, κ, de la intensidad del campo magnético.

Wang et al. (2015) [74] enfocaron su análisis en la parte anterior de la onda de tsunami, usando valores del nivel de mar provenientes de cuatro mareógrafos virtuales ubicados dos grados alrededor de la Isla de Pascua, ya que la Ec. 4.2 solo es válida en lugares donde la columna de agua no experimenta variaciones importantes en la dirección horizontal en comparación con el campo de velocidades; es decir, mar adentro, lejos de las plataformas continentales y líneas de costa. Esta restricción aparece al no considerar los términos $\partial_x D$ y $\partial_y D$ del lado izquierdo de la Ec. 2.11. Por otra parte, el modelo desarrollado en esta tesis considera datos de cada punto de grilla, incluso en los cuales la batimetría puede cambiar abruptamente. Esto podría explicar el ajuste del modelo a los datos, por lo menos en la parte anterior de la onda (Fig. 4.2).

Aunque con los resultados de esta tesis no se espera describir una eventual atenuación de b_z causada por el campo eléctrico inducido en la ley de Faraday (el cual se opone al término $\vec{u} \times \vec{F}$), algunos comentarios en relación a este tema son necesarios. Tomando el rotor de la Ec. 2.3, combinando con la Ec. 2.2, y asumiendo una conductividad homogénea, se obtiene la ecuación de inducción magnética, Ec. 4.3, donde $K = (\mu_0 \sigma_s)^{-1}$. El término generador, $\nabla \times (\vec{u} \times \vec{B})$, es balanceado por el término relacionado con la auto-inducción, $\partial_t \vec{B}$, y el término relacionado con la disipación magnética, $\nabla \times (K \nabla \times \vec{B})$. La dependencia de la Ec. 4.3 con la profundidad del océano para el caso de un tsunami fue investigada por Minami et al. (2015) [46], quienes usaron cálculos numéricos en dos dimensiones y en el dominio del tiempo. La dependencia fue estudiada en base al número magnético de Reynolds (Eq. 4.4), el cual compara la magnitud relativa de los dos términos en el lado derecho de la Ec. 4.3 (Bittencourt 2004 [7]). En la Ec. 4.4, U y L son escalas típicas de velocidad y longitud, respectivamente, del movimiento. Usando $U = \sqrt{gH}$ y $L = H$, Minami et al. (2015) [46] encontraron que la influencia del término difusivo disminuye al aumentar la profundidad de la capa oceánica, mientras que el término de auto-inducción debe aumentar su magnitud para balancear el término generador.

Reemplazando $U = L/T$, donde T es una escala de tiempo, y usando la longitud de onda en lugar de la profundidad como escala de longitud en la Ec. 4.4, el efecto de auto-inducción pierde importancia en flujos subinerciales (como los relacionados con las Figs. 4.10- 4.18). Por ejemplo, usando $L = 200$ km y $T = 20$ días, se obtiene Rm =0.1. Por otra parte, para un tsunami con valores típicos de $L = 100$ km y $T = 20$ min, $Rm = 42 \gg 1$, lo cual corresponde a un caso en el que domina la auto-inducción por sobre la difusión. El uso de la longitud de onda, en lugar de la

profundidad, como escala de longitud coincide con lo realizado en trabajos previos (Podney 1975 [49]; Chave y Luther 1990 [12]), y el efecto de auto-inducción debería ser considerado en el caso de un tsunami.

En las Figs. 4.19- 4.20 se muestran comparaciones entre mediciones en IPM durante los dos tsunamis, y los modelos desarrollados en esta tesis y en Tatehata et al. (2015) [61], cuyo mecanismo considera el término asociado a la auto-inducción al resolver la Ec. 4.3 para b_z usando condiciones de borde apropiadas. Tatehata et al. (2015) [61] calcularon las corrientes eléctricas en cada punto de grilla basándose en la solución analítica de Tyler (2005) [65], y posteriormente integraron los campos magnéticos inducidos usando la ley de Biot-Savart. La aplicación de su mecanismo en este trabajo manteniendo la resolución de 0.27 arcmin en la grilla del segundo nivel demandaba un gran costo computacional. Por lo tanto, para dicho nivel, solo se consideró una grilla de 1.08 arcmin. No se observaron mejoras significativas en el ajuste entre los datos y los nuevos resultados, lo que puede deberse al hecho de que la auto-inducción comienza a disminuir a medida que lo hace la profundidad (específicamente, con profundidades $H < 5$ km), de acuerdo con la Fig. 4 de Minami et al. (2015) [46]. Por lo tanto, la elección de un modelo magnetostático en esta tesis parece razonable.

Dado que la temperatura del océano disminuye con la profundidad, un perfil de conductividad eléctrica más cercano a la realidad, en lugar de un valor homogéneo, podría influir en los resultados. Por ejemplo, un perfil de conductividad que varía en forma radial implicaría usar un "transporte horizontal de conductividad", $\sigma_s \vec{u}_H$, a través de la Ec. 4.5, para calcular las Ecs. 3.2 (Sanford 1971 [54]). Esta consideración

es importante cuando se investigan procesos que alteran la salinidad y el calor en el océano. Petereit et al. (2018) [48] compararon cálculos de temperatura en el océano con perturbaciones magnéticas usando un período de tiempo de 50 años, encontrando que estas últimas contenían información suficiente como para predecir fases frías y cálidas asociadas a El Niño-Oscilación Sur. Estas fases están relacionadas con grandes fluctuaciones de temperatura en el océano, las cuales a su vez implican un cambio en el perfil de conductividad eléctrica. Obviamente, estos procesos están más relacionados con los resultados mostrados en las Figs. 4.7- 4.18 que con los asociados a eventos de tsunami.

Además de la influencia de una conductividad dependiente de la profundidad, cambios abruptos de este parámetro en la dirección horizontal (por ejemplo, entre el océano y tierra) también podrían modificar los resultados. Usando la Ec. 4.3 y separando la resistividad, $1/\sigma_s$, en sus componentes radial y lateral, un campo poloidal secundario, generado a partir de la componente toroidal, se acopla a las mediciones originales del campo poloidal en observatorios magnéticos cercanos a la costa (Velímský et al. 2019 [72]). A pesar de que en su estudio del 2014, Zhang et al. (2014) [79] encontraron que este efecto era despreciable en mediciones realizadas en una isla cercana a Japón durante el tsunami de Japón 2011, la transferencia de energía desde el modo TM al PM a causa de cambios laterales en la conductividad eléctrica podría ser investigada en el futuro usando datos de IPM.

Tal como se sugirió en la Introducción, los datos de IPM son una prometedora fuente de información para estudiar la actividad oceánica en el giro subtropical del Pacífico sur, debido a la estratégica posición de la isla. Por ejemplo, basado en la

Ec. 4.5, y utilizando la misma región alrededor de la isla y los datos de IPM, cambios en las distribuciones de temperatura y salinidad podrían ser monitoreados usando OMCT, que calcula distribuciones de salinidad, temperatura y velocidades como fuentes de inducción de campos magnéticos (ver Saynisch et al. 2016 [57]; Irrgang et al. 2018 [23]). Una futura refinación del modelo de esta tesis usando OMCT podría llevar a una mejora de los actuales resultados.

Comparaciones de campos magnéticos inducidos usando distintas fuentes de datos, por ejemplo, índices planetarios de actividad geomagnética, podrían complementar el uso de modelos numéricos, y entregar pistas sobre intervalos de tiempo en los cuales la influencia de procesos oceánicos sea más probable. Un ejemplo son los valores Ap (Fig. 4.21), que pueden ser considerados como una medida de las emisiones corpusculares del Sol a través de su efecto magnético en la Tierra (Ahluwalia 1998 [1]). En general, las curvas de la Fig. 4.21 tienen formas y órdenes de magnitud similares, a pesar de algunos valores extremos de Ap e intervalos de tiempo en los cuales las diferencias son más notables. Algunas diferencias podrían ser explicadas por la influencia de corrientes oceánicas bajo los 500 m, tal como se mencionó en la página 32.

REFERENCES

[1] H. S. Ahluwalia. The predicted size of cycle 23 based on the inferred three-cycle quasi-periodicity of the planetary index ap. *Journal of Geophysical Research: Space Physics*, 103(A6):12103–12109, 1998.

[2] Isabel Andrade, Samuel Hormazábal, and Marco Correa-Ramírez. Time-space variability of satellite chlorophyll-a in the easter island province, southeastern pacific ocean. *Latin american journal of aquatic research*, 42(4):871–887, 2014.

[3] John R. Apel. *Principles of Ocean Physics*. Academic Press, London, 1999.

[4] Yefei Bai, Yoshiki Yamazaki, and Kwok Fai Cheung. Interconnection of multi-scale standing waves across the pacific basin from the 2011 tohoku tsunami. *Ocean Modell.*, 92:183–197, 2015.

[5] G. Bellotti, R. Briganti, and G. M. Beltrami. The combined role of bay and shelf modes in tsunami amplification along the coast. *Journal of Geophysical Research: Oceans*, 117(C8):n/a–n/a, 2012. C08027.

[6] Roberto Benavente, Phil R. Cummins, and Jan Dettmer. Rapid automated w-phase slip inversion for the illapel great earthquake (2015, mw = 8.3). *Geophysical Research Letters*, 43(5):1910–1917, 2016.

[7] J.A. Bittencourt. *Fundamentals of Plasma Physics*. Springer-Verlag New York, Inc., 3 edition, 2004.

[8] Ignacia Calisto, Matthew Miller, and Iván Constanzo. Comparison between tsunami signals generated by different source models and the observed data of the illapel 2015 earthquake. *Pure Appl. Geophys.*, 173(4):1051–1061, 2016.

[9] Wallace H. Campbell. *Introduction to Geomagnetic Fields*. Cambridge University Press, New York, USA, 2 edition, 2003.

[10] Alan D. Chave. On the theory of electromagnetic induction in the earth by ocean currents. *Journal of Geophysical Research: Solid Earth*, 88(B4):3531–3542, 1983.

[11] Alan D. Chave, Jean H. Filloux, and Douglas S. Luther. Electromagnetic induction by ocean currents: Bempex. *Phys. Earth Planet. Inter.*, 53(3):350 – 359, 1989.

[12] Alan D. Chave and Douglas S. Luther. Low-frequency, motionally induced electromagnetic fields in the ocean: 1. theory. *Journal of Geophysical Research: Oceans*, 95(C5):7185–7200, 1990.

[13] Benoit Cushman-Roisin. *Introduction to Geophysical Fluid Dynamics*. Prentice-Hall, Inc., Englewood Cliffs, New Jersey, USA, 1994.

[14] Benoit Cushman-Roisin and Jean-Marie Beckers. *Introduction to Geophysical Fluid Dynamics: Physical and Numerical Aspects*. Academic Press, 2 edition, 2011.

[15] William J. Emery and Richard E. Thomson. *Data Analyis Methods in Physical Oceanography*. Elsevier, Amsterdam, 2001.

[16] S. Glimsdal, G. K. Pedersen, C. B. Harbitz, and F. Løvholt. Dispersion of tsunamis: does it really matter? *Nat. Hazards Earth Syst. Sci.*, 13(6):1507–1526, 2013.

[17] WD Gonzalez, Jo-Ann Joselyn, Yohsuke Kamide, Herb W Kroehl, G Rostoker, BT Tsurutani, and VM Vasyliunas. What is a geomagnetic storm? *Journal of Geophysical Research: Space Physics*, 99(A4):5771–5792, 1994.

[18] David J. Griffiths. *Introduction to Electrodynamics*. Cambridge University Press, United Kingdom, 4 edition, 2013.

[19] A. Grinsted, J. C. Moore, and S. Jevrejeva. Application of the cross wavelet transform and wavelet coherence to geophysical time series. *Nonlinear Processes in Geophysics*, 11(5/6):561–566, November 2004.

[20] K Hasselmann. An ocean model for climate variability studies. *Progress in Oceanography*, 11(2):69–92, 1982.

[21] Juan Horrillo, Zygmunt Kowalik, and Yoshinori Shigihara. Wave dispersion study in the indian ocean-tsunami of december 26, 2004. *Marine Geodesy*, 29(3):149–166, 2006.

[22] C. Irrgang, J. Saynisch, and M. Thomas. Estimating global ocean heat content from tidal magnetic satellite observations. *Scientific Reports*, 9(1):7893, 2019.

[23] C. Irrgang, J. Saynisch-Wagner, and M. Thomas. Depth of origin of ocean-circulation-induced magnetic signals. *Annales Geophysicae*, 36(1):167–180, 2018.

[24] I. Kawashima and H. Toh. Tsunami-generated magnetic fields may constrain focal mechanisms of earthquakes. *Sci. Rep.*, 6:28603, June 2016.

[25] E. A. Kherani, P. Lognonné, H. Hébert, L. Rolland, E. Astafyeva, G. Occhipinti, P. Coïsson, D. Walwer, and E. R. de Paula. Modelling of the total electronic content and magnetic field anomalies generated by the 2011 Tohoku-Oki tsunami and associated acoustic-gravity waves. *Geophysical Journal International*, 191(3):1049–1066, 12 2012.

[26] E.A. Kherani, L. Rolland, P. Lognonné, A. Sladen, V. Klausner, and E.R. de Paula. Traveling ionospheric disturbances propagating ahead of the tohoku-oki tsunami: a case study. *Geophys. J. Int.*, 204(2):1148, 2016.

[27] V. Klausner, T. Almeida, F. C. de Meneses, E. A. Kherani, V. G. Pillat, and M. T. A. H. Muella. Chile2015: Induced magnetic fields on the z component by tsunami wave propagation. *Pure Appl. Geophys.*, 173(5):1463–1478, 2016.

[28] V. Klausner, T. Almeida, F. C. de Meneses, E. A. Kherani, V. G. Pillat, M. T. A. H. Muella, and P. R. Fagundes. First report on seismogenic magnetic disturbances over brazilian sector. *Pure Appl. Geophys.*, 174(3):737–745, 2017.

[29] V. Klausner, Odim Mendes, Margarete O. Domingues, Andres R. R. Papa, Robert H. Tyler, Peter Frick, and Esfhan A. Kherani. Advantage of wavelet technique to highlight the observed geomagnetic perturbations linked to the chilean tsunami (2010). *Journal of Geophysical Research: Space Physics*, 119(4):3077–3093, 2014.

[30] Keith D. Koper, Alexander R. Hutko, Thorne Lay, and Oner Sufri. Imaging short-period seismic radiation from the 27 february 2010 chile (mw 8.8) earthquake by back-projection of p, pp, and pkikp waves. *Journal of Geophysical Research: Solid Earth*, 117(B2), 2012.

[31] Pijush K. Kundu and Ira M. Cohen. *Fluid Mechanics*. Elsevier/Academic Press, 4 edition, 2008.

[32] J. C. Larsen. Electric and magnetic fields induced by deep sea tides. *Geophys. J. Int.*, 16(1):47, 1968.

[33] Paul H. LeBlond and Lawrence A. Mysak. *Waves in the Ocean*. Elsevier Science Publishing Company Inc., 1 edition, 1978.

[34] Boris W. Levin and Mikhail A. Nosov. *Physics of Tsunamis*. Springer International Publishing, 2016.

[35] MS Longuet-Higgins. On the trapping of wave energy round islands. *Journal of Fluid Mechanics*, 29(4):781–821, 1967.

[36] Lilley F. E. M., Filloux J. H., Mulhearn P. J., and Ferguson I. J. Magnetic signals from an ocean eddy. *Journal of geomagnetism and geoelectricity*, 45(5):403–422, 1993.

[37] C. Manoj, A. Kuvshinov, S. Maus, and H. Lühr. Ocean circulation generated magnetic signals. *Earth, Planets and Space*, 58(4):429–437, Apr 2006.

[38] Chandrasekharan Manoj, Stefan Maus, and Arnaud Chulliat. Observation of magnetic fields generated by tsunamis. *Eos, Transactions American Geophysical Union*, 92(2):13–14, 2011.

[39] Charles R McClain, Sergio R Signorini, and James R Christian. Subtropical gyre variability observed by ocean-color satellites. *Deep Sea Research Part II: Topical Studies in Oceanography*, 51(1):281 – 301, 2004. Views of Ocean Processes from the Sea-viewing Wide Field-of-view Sensor (SeaWiFS) Mission: Volume 1.

[40] Chiang C. Mei, Michael Stiassnie, and Dick K.-P. Yue. *Theory and Applications of Ocean Surface Waves*, volume 23 of *Advances Series on Ocean Engineering*. World Scientific Publishing Co. Pte. Ltd., 2005.

[41] M. Menvielle and A. Berthelier. The k-derived planetary indices: Description and availability. *Reviews of Geophysics*, 29(3):415–432, 1991.

[42] Takuto Minami. Motional induction by tsunamis and ocean tides: 10 years of progress. *Surv. Geophys.*, Jun 2017.

[43] Takuto Minami, Tungcheng Ho, Zhiheng Lin, and Hiroaki Toh. Can we detect tsunami magnetic signals at on-land observations prior to tsunami arrivals?: From the perspective of numerical experiments. *Poster presented at the Japan Geophysical Union Conference 2019, Chiba, Japan*, 05 2019.

[44] Takuto Minami and Hiroaki Toh. Two-dimensional simulations of the tsunami dynamo effect using the finite element method. *Geophysical Research Letters*, 40(17):4560–4564, 2013.

[45] Takuto Minami, Hiroaki Toh, Hiroshi Ichihara, and Issei Kawashima. Three-dimensional time domain simulation of tsunami-generated electromagnetic fields: Application to the 2011 tohoku earthquake tsunami. *Journal of Geophysical Research: Solid Earth*, 122(12):9559–9579, 2017.

[46] Takuto Minami, Hiroaki Toh, and Robert H. Tyler. Properties of electromagnetic fields generated by tsunami first arrivals: Classification based on the ocean depth. *Geophys. Res. Lett.*, 42(7):2171–2178, 2015. 2015GL063055.

[47] Sophie Munger and Kwok Fai Cheung. Resonance in hawaii waters from the 2006 kuril islands tsunami. *Geophys. Res. Lett.*, 35(7), 2008.

[48] J. Petereit, J. Saynisch, C. Irrgang, T. Weber, and M. Thomas. Electromagnetic characteristics of enso. *Ocean Science*, 14(3):515–524, 2018.

[49] Walter Podney. Electromagnetic fields generated by ocean waves. *J. Geophys. Res.*, 80(21):2977–2990, 1975.

[50] A Poupardin, P Heinrich, H Hébert, F Schindelé, A Jamelot, D Reymond, and H Sugioka. Traveltime delay relative to the maximum energy of the wave train for dispersive tsunamis propagating across the pacific ocean: the case of 2010 and 2015 chilean tsunamis. *Geophysical Journal International*, 214(3):1538–1555, 2018.

[51] A. T. Price. Electromagnetic induction in a semi-infinite conductor with a plane boundary. *Q J Mechanics Appl Math*, 3(4):385–410, 1950.

[52] L. D. Pukhtyar and A. S. Kukushkin. Investigation of the electromagnetic fields induced by sea wave motion. *Phys. Oceanogr.*, 7(1):33–41, 1996.

[53] Guillermo Rubilar. Electrodinámica. *Apuntes de clase recuperados el 16 de julio de 2016 desde el sitio web del curso: Electrodinámica, del Departamento de Ciencias Físicas, Universidad de Concepción, Chile: http://electrodinamica1-udec-2016-2.blogspot.com/*, 2016.

[54] Thomas Sanford. Motionally induced electric and magnetic fields in the sea. *J. Geophys. Res.*, 76(15):3476–3492, may 1971.

[55] J. Saynisch, C. Irrgang, and M. Thomas. On the use of satellite altimetry to detect ocean circulation's magnetic signals. *Journal of Geophysical Research: Oceans*, 123(3):2305–2314, 2018.

[56] J. Saynisch, J. Petereit, C. Irrgang, and M. Thomas. Impact of oceanic warming on electromagnetic oceanic tidal signals: A cmip5 climate model-based sensitivity study. *Geophysical Research Letters*, 44(10):4994–5000, 2017.

[57] Jan Saynisch, J Petereit, Christopher Irrgang, Alexey Kuvshinov, and Maik Thomas. Impact of climate variability on the tidal oceanic magnetic signal—a model-based sensitivity study. *Journal of Geophysical Research: Oceans*, 121(8):5931–5941, 2016.

[58] N. R. Schnepf, C. Manoj, C. An, H. Sugioka, and H. Toh. Time–frequency characteristics of tsunami magnetic signals from four pacific ocean events. *Pure Appl. Geophys.*, 173(12):3935–3953, 2016.

[59] Neesha R Schnepf, Manoj Nair, Astrid Maute, Nicholas M Pedatella, Alexey Kuvshinov, and Arthur D Richmond. A comparison of model-based ionospheric

and ocean tidal magnetic signals with observatory data. *Geophys. Res. Lett.*, 45(15):7257–7267, 2018.

[60] V. M. Sorokin, A. K. Yashchenko, and V. V. Surkov. Generation of geomagnetic disturbances in the ionosphere by a tsunami wave. *Geomagnetism and Aeronomy*, 59(2):221–233, Mar 2019.

[61] Hidee Tatehata, Hiroshi Ichihara, and Yozo Hamano. Tsunami-induced magnetic fields detected at chichijima island before the arrival of the 2011 tohoku earthquake tsunami. *Earth, Planets and Space*, 67(1):185, Nov 2015.

[62] Stefano Tinti and Cesare Vannini. Theoretical investigation on tsunamis induced by seismic faults near ocean islands. *Mar. Geod.*, 17(3):193–212, 1994.

[63] Christopher Torrence and Gilbert P. Compo. A practical guide to wavelet analysis. *Bull. Amer. Meteor. Soc.*, 79(1):61–78, 1998.

[64] Carlos E. Torres, Ignacia Calisto, and Dante Figueroa. Magnetic signals at easter island during the 2010 and 2015 chilean tsunamis compared with numerical models. *Pure and Applied Geophysics*, 176(7):3167–3183, Jul 2019.

[65] R. H. Tyler. A simple formula for estimating the magnetic fields generated by tsunami flow. *Geophys. Res. Lett.*, 32(9):n/a–n/a, 2005. L09608.

[66] R. H. Tyler. Weak influences of the earth's magnetic field on ocean circulation. *Geophys. Res. Lett.*, 33(14), 2006.

[67] R.H. Tyler, S. Maus, and H. Lühr. Satellite observations of magnetic fields due to ocean tidal flow. *Science*, 299(5604):239–241, 2003.

[68] RH Tyler, JM Oberhuber, and TB Sanford. The potential for using ocean generated electromagnetic fields to remotely sense ocean variability. *Physics and Chemistry of the Earth, Part A: Solid Earth and Geodesy*, 24(4):429–432, 1999.

[69] Robert H Tyler, Tim P. Boyer, Takuto Minami, Melissa M. Zweng, and James R. Reagan. Electrical conductivity of the global ocean. *Earth Planets Space*, 69(156), 2017.

[70] Robert H Tyler and Lawrence A Mysak. Electrodynamics in a rotating frame of reference with application to global ocean circulation. *Canadian journal of physics*, 73(5-6):393–402, 1995.

[71] Robert H Tyler and Lawrence A Mysak. Motionally-induced electromagnetic fields generated by idealized ocean currents. *Geophys. Astrophys. Fluid Dynamics*, 80(3-4):167–204, 1995.

[72] Jakub Velímský, Libor Šachl, and Zdeněk Martinec. The global toroidal magnetic field generated in the earth's oceans. *Earth and Planetary Science Letters*, 509:47 – 54, 2019.

[73] Peter von Dassow and Silvana Collado-Fabbri. Biological oceanography, biogeochemical cycles, and pelagic ecosystem functioning of the east-central south pacific gyre: focus on easter island and salas y gómez island. *Latin american journal of aquatic research*, 42(4):703–742, 2014.

[74] Benlong Wang, Xiaoyu Guo, Hua Liu, and Cheng Gong. On the magnetic anomaly at easter island during the 2010 chile tsunami. *Theor. Appl. Mech. Lett.*, 5(5):187–190, August 2015.

[75] Benlong Wang and Hua Liu. Space-time behaviour of magnetic anomalies induced by tsunami waves in open ocean. *Proceedings of the Royal Society of London A: Mathematical, Physical and Engineering Sciences*, 469(2157), 2013.

[76] Xiaoming Wang. User manual for comcot version 1.7 (first draft). 2009.

[77] J. T. Weaver. The General Theory of Electromagnetic Induction in a Conducting Half-Space. *Geophys. J. Int.*, 22(1):83–100, 01 1971.

[78] Yoshiki Yamazaki and Kwok Fai Cheung. Shelf resonance and impact of near-field tsunami generated by the 2010 chile earthquake. *Geophys. Res. Lett.*, 38(12):n/a–n/a, 2011. L12605.

[79] Luolei Zhang, Hisashi Utada, Hisayoshi Shimizu, Kiyoshi Baba, and Takuto Maeda. Three-dimensional simulation of the electromagnetic fields induced by the 2011 tohoku tsunami. *Journal of Geophysical Research: Solid Earth*, 119(1):150–168, 2014. 2013JB010264.